

# **Origin and nature of killer defects in 3C-SiC for power electronic applications by a multiscale atomistic approach**

Emilio Scalise<sup>a</sup>, Luca Barbisan<sup>a</sup>, Andrey Sarikov<sup>a, b</sup>, Francesco Montalenti<sup>a</sup>, Leo Miglio<sup>a</sup>, and Anna Marzegalli<sup>a, c, \*</sup>

<sup>a</sup> *L-NESS and Department of Materials Science, Università degli Studi di Milano-Bicocca, via Cozzi 55, I-20125, Milano, Italy*

<sup>b</sup> *V. Lashkarev Institute of Semiconductor Physics, National Academy of Sciences of Ukraine, 45 Nauki avenue, 03028 Kyiv, Ukraine*

<sup>c</sup> *L-NESS and Department of Physics, Politecnico di Milano, via Anzani 42, I-22100, Como, Italy*

*\* Corresponding author. Phone: +39 02 6448 5212*

*E-mail addresses:*

*emilio.scalise@unimib.it, l.barbisan@campus.unimib.it, andrey.sarikov@unimib.it, francesco.montalenti@unimib.it, leo.miglio@unimib.it, anna.marzegalli@unimib.it*

## **ABSTRACT**

3C-SiC epitaxially grown on Si displays a large wealth of extended defects. In particular, single, double and triple stacking faults (SFs) are observed in several experiments to coexist. Overabundance of defects has so far limited the exploitation of 3C-SiC/Si for power electronics, in spite of its several ideal properties (mainly in terms of wide gap, high breakdown fields and thermal properties) and the possibility of a direct integration in the Si technology.

Here we use a multiscale approach, based on both classical molecular dynamics (MD) simulations and first-principle calculations, to investigate in-depth the origin, nature and properties of most common 3C-SiC/Si(001) extended defects.

Our MD simulations reveal a natural path for the formation of partial dislocation complexes terminating both double and triple SF's. MD results are used as input for superior DFT calculations, allowing us to better determine the core structure and to investigate electronic properties. It turns out that the partial dislocation complexes terminating double and triple SFs are responsible for the introduction of electronic states significantly filling the band gap. On the other hand, individual partial dislocations terminating single SFs only induce states very close to the gap edge. We conclude that partial dislocation complexes, in particular the most abundant triple ones, are killer defects in terms of favoring leakage currents. Suggestions coming from theory/simulations for devising a strategy to lower their occurrence are discussed.

*Keywords:* 3C-SiC, Silicon carbide, Stacking faults, Dislocations, Atomistic simulations

## **1. Introduction**

SiC is a group IV compound with unique physical and chemical properties, mainly conditioned by the strong tetrahedral bonding between Si and C atoms (4.6 eV). It is a wide bandgap material (2.3-3.3 eV, depending on the crystal phases), which possesses excellent thermal stability (sublimation temperatures up to 2800°C), high thermal conductivity (3.2-4.9 W/cm K, about three times higher than the one of Si), high breakdown field ( $30 \times 10^5$  V/cm, about ten times higher than that for Si),

large carrier saturation velocity ( $2 \times 10^7$  cm/s), hardness (Knoop hardness of 2480 kg/mm<sup>2</sup>), and chemical inertness [1-3]. Therefore, the hexagonal phases of SiC are increasingly used for electronic devices operating at elevated temperatures, large power and high frequencies, as well as in harsh environments [4]. Beyond the tetrahedral coordination at first neighbours, silicon and carbon atoms in SiC may occupy different lattice positions at further neighbours, giving rise to multiple crystal structures [5-7]. In particular, the most common SiC polytypes are the hexagonal 6H and 4H phases, and the cubic 3C structure, with a stability hierarchy depending on temperature, as recently understood in our recent paper [7]. The 3C-SiC cubic phase is the natural output of deposition processes on Si substrates and displays several interesting features. First, it has excellent electrical properties, such as a reduced phonon scattering resulting from the high symmetry of this material, as well as the highest electron mobility and saturated drift velocity, when compared to other SiC polytypes. Second, 3C-SiC may be used as a substrate for the epitaxial growth of relevant materials, such as gallium nitride [8] and boron nitride [9].

Currently, the growth of large area bulk 3C-SiC material is still in progress, however it can be also deposited on hexagonal SiC substrates (4H and 6H). Unfortunately, commercially available wafers of hexagonal SiC are small, much smaller than the Si ones, and their crystal quality is not sufficiently good as well. They contain a large number of defects that may propagate in the 3C-SiC epilayers [10]. As already mentioned, cubic silicon carbide layers can be heteroepitaxially grown on (001) and (111) silicon substrates, enabling direct integration into the Si technology [11] and thus offering an advantage over other SiC polytypes. Still, structural and thermal differences between the substrate and epilayer hinder the possibility to obtain high quality crystalline 3C-SiC on Si substrates, thus reducing

the high theoretical potential of this material for power electronics. In particular, the lattice parameters of cubic silicon carbide and silicon (4.53 Å and 5.43 Å, respectively, at room temperature) differ by about 20 %, and their thermal expansion coefficients by 8 %. Thus, both during the high temperature deposition and the cooling down, several types of defects, such as dislocations, twins and stacking faults nucleate at or close to the 3C-SiC/Si interface and propagate into the 3C-SiC films, as driven by the misfit strain relaxation [12, 13]. Such defects have detrimental effects on the performance of devices, particularly on the leakage current and breakdown electric field. In details, the correlation of the latter characteristics with twins and stacking faults in the epitaxial 3C-SiC films has been observed experimentally in a number of publications [14- 21]. As a consequence, although the Si substrates are regarded as the most convenient choice for 3C-SiC epitaxy at the moment, the high-quality growth is still an important challenge for researchers.

A common strategy to reduce the 3C-SiC and Si lattice misfit strain at the early stage of the Si carbide epitaxy is the so-called carbonization process, realized by a deposition of carbon-rich precursors under hydrogen flux [22, 23]. Release of strain and associated stress takes place by different mechanisms, depending on the specific carbonization procedure and the substrate orientation [24-26]. As a result of this procedure, only some residual strain remains in the layer, where the sign and the magnitude depend on the deposition parameters [25]. In most cases, an array of ordered misfit sessile dislocations appears at the 3C-SiC/Si substrate interface, allowing to match five SiC unit cells to four Si lattice units [26, 27] and leaving a slightly compressed 3C-SiC layer (at the growth temperature) for the subsequent deposition [28]. The carbonization step does improve the crystal quality of 3C-SiC layers, however, it does not reduce the defect density to such an extent to ensure

acceptable quality (i.e. stacking fault density to  $10^2/\text{cm}$ ) level for device performance [17, 27, 29].

In addition to sessile dislocation arrays formed at the 3C-SiC/Si interface, the stress in the epitaxial layer is partially released by a nucleation and evolution of the partial dislocations accompanying the appearance of single and multiple stacking faults (SFs) in the 3C-SiC films, as favored by SiC polytypism. In fact, hexagonal phases become favored at high deposition temperatures ( $T=1200-1400^\circ\text{C}$ ) and inclusion of hexagonal polytypes in 3C-SiC effectively corresponds to the multi-plane stacking faults in the cubic lattice [7, 30]. These multiple stacking faults in cubic silicon carbide are predicted to have lower formation energies at any temperature, as compared to the single-plane SF [7], and indeed their abundance in 3C-SiC epitaxial layers is confirmed experimentally [26, 27, 31, 32].

The observed direct correlation between the stacking fault density and the leakage current values in 3C-SiC layers [14-21], discussed above, drove several difficult attempts in finding the way for their reduction [18, 21, 33, 34, 35, 36]. Actually, it is an open question whether the SFs per se are responsible for the detrimental leakage currents, because they are theoretically predicted to introduce no mid-gap electronic states in 3C-SiC phase [37, 38]. Instead, partial dislocations and dislocation complexes, bounding the stacking faulted regions to the rest of the 3C-SiC crystal, may be well considered as suitable candidates for the killing defects in 3C-SiC, inducing leakage currents in this material.

In this paper, we use a multiscale approach combining classical molecular dynamics (MD) simulations and ab initio calculations, to study the formation mechanisms and electronic properties of the complexes of partial dislocations in 3C-SiC epitaxial layers. We show that the strain conditions developed in the early

deposition stages enhance the probability of obtaining three partial dislocations in adjacent planes, terminating a triple stacking fault, in agreement with experimental indications [39]. The attractive interaction between the dislocations induces the formation of stable complexes, which are particularly interesting for the transport properties. In fact, a detailed analysis of the electronic properties of single partial dislocations, as well as dislocation complexes, is performed by ab initio calculations, demonstrating the appearance of the band of states in the middle of the band gap of 3C-SiC in the case of double and triple partial dislocation complexes.

The paper is organized as follows. In Section 2, we describe the simulation technical details for both molecular dynamics (MD) (Subsection 2.1) and ab initio calculation (Subsection 2.2). Section 3 presents the discussion of obtained results and is divided in two parts. The results on the origin of the dislocation complexes and their final structure obtained by MD simulations are reported in Subsection 3.1 both in a simplified two dimensional view (Subsection 3.1.1) and in a more complex three dimensional full line description (Subsection 3.1.2). In Subsection 3.2, the electronic properties of the partial dislocation complexes terminating single (Subsection 3.2.1), double (Subsection 3.2.2) and triple (Subsection 3.2.3) stacking faults obtained by ab initio calculations, are shown. Finally, we draw conclusions to the paper in Section 4.

## **2. Methodology**

### *2.1. Molecular Dynamics*

The evolution of partial dislocations and the formation of dislocation complexes terminating the stacking faults in 3C-SiC have been simulated by molecular dynamics, employing the Large-scale Atomic/Molecular Massively Parallel

Simulator (LAMMPS) [40]. The simulations have been performed mainly within the Vashishta potential [41], which has some advantages over the few empirical potentials fitted on SiC parameters. In particular, this potential takes into account the interactions beyond the first neighbour shell, therefore it provides a different total energy for the hexagonal versus the cubic configuration, thus enabling to compute one empirical estimate of SF energies. Moreover, the comparatively longer times for individual step computation is compensated by the possibility to choose significantly larger time step values, as compared to other potentials (e.g. 1 fs ensuring relative energy conservation to  $10^{-5}$ ). The main results of our simulations have been also verified by additional simulations using the Analytic Bond Order Potential (ABOP) [42], which is complementary to the Vashista potential, according to the analysis outlined in [43].

The simulations have been performed within the framework of the Nose-Hoover thermostat. Positions and velocities of atoms have been sampled from the canonical (NVT) ensemble and obtained from non-Hamiltonian equations of motion [44]. The atomic trajectories have been analyzed using the Open Visualization Tool (OVITO) software [45], which enables to resolve extended defects in virtual crystals, highlighting SFs and providing dislocation lines with the associated Burgers vectors. The simulation cell has been composed as an orthogonal box defined by  $\vec{s} = \frac{a}{2}[1\bar{1}0]$ ,  $\vec{v} = \frac{a}{2}[110]$ ,  $\vec{w} = a[001]$ . Periodic boundary conditions have been applied in the  $\vec{s}$  and  $\vec{v}$  directions to model an infinitely large slab of 3C-SiC. To model the effect of a thick bulk substrate in the 3C-SiC layer, the bottom atoms in the simulation cell have been kept immobile, while the free surface condition (surface atoms exposed to vacuum) has been set on the opposite side along the  $\vec{w}$  direction (top part of the cell). Box dimensions have been chosen in order to ensure the optimum balance between

the computational cost and the accuracy in the description of dislocation gliding in the considered systems.

Dislocations have been inserted in the simulation cell by shifting each atom according to the displacement field vectors calculated within the dislocation modelling in the framework of the linear elasticity theory [46]. For an arbitrary dislocation, the field components can be easily calculated rotating the reference system and decomposing the dislocation Burgers vector into a screw ( $b_{//}$ ) and an edge component ( $b_{\perp}$ ). At this,  $\hat{z}$  axis has to be oriented along the dislocation line  $\vec{\xi}$ ,  $\hat{x}$  axis has to be perpendicular to  $\vec{\xi}$  in the glide plane, and  $\hat{y}$  axis oriented following the right hand rule, respectively. In this case, the components of the displacement field vectors can be written as follows:

$$u_x(x, y, z) = \frac{b_{\perp}}{2\pi} \left( \arctan\left(\frac{y}{x}\right) + \frac{xy}{2(1-\nu)(x^2+y^2)} \right) \quad (1)$$

$$u_y(x, y, z) = -\frac{b_{\perp}}{2\pi} \left( \frac{(1-2\nu)}{4(1-\nu)} \ln(x^2 + y^2) + \frac{x^2 - y^2}{4(1-\nu)(x^2 + y^2)} \right) \quad (2)$$

$$u_z(x, y, z) = \frac{b_{//}}{2\pi} \arctan\left(\frac{y}{x}\right) \quad (3)$$

where  $\nu = 0.25$  is the Poisson ratio of 3C-SiC [47].

Having a free surface and, in fact, a periodic array of dislocations, some corrections to the displacement field are needed. First, the stress normal to free surface should be zero after system equilibration. In order to save computational time, we have added image dislocations in the vacuum above the free surface [46]. Second, as proved in [48], the equations above if summed in an infinite series turn to be conditionally convergent, so that a correction to the displacement field in the plane  $\hat{x}\hat{y}$  is needed to account for an infinite array of parallel dislocations [49].

As a first stage, we considered infinitely long and straight dislocation lines with  $\vec{\xi} // \vec{v}$  (simulation set called A in the following). The simulation cell was composed of 40320 atoms arranged in the  $21.6 \times 1.23 \times 15.7 \text{ nm}^3$  box. The box dimension along the direction of the vector  $\vec{s}$  has been chosen so that a specific strain was present in the cell after the insertion of dislocations (see Section 3). In the direction of the vector  $\vec{v}$ , the box was narrower to reduce the computational cost, being at the same time large enough to allow kink formation and migration during dislocation gliding. We tested the appropriateness of the box dimension in this direction: three times increase of this value did not effect on the motion of dislocations. The number of atomic layers in the direction of the vector  $\vec{w}$  was chosen in order to have the dislocation far enough from both the fixed atoms at the bottom part of the simulation cell, and from the free surface in its top part. A series of simulations has been performed varying the number of atomic monolayers and the distances of dislocations from the surface. The best description was obtained for the 144 monolayers in the direction of the vector  $\vec{w}$  of simulation cell.

Next we developed simulations showing three dimensional evolution of hexagonal dislocation loops (see Section 3.1.2.1). In order to allow extension of dislocation loops we were forced to use a larger cell with respect to the case of the straight line dislocations, still keeping the same orientation. A box comprising 3369528 atoms ( $38.8 \times 38.8 \times 26.0 \text{ nm}^3$ ) has been created. In the following these set up is called simulation set B.

Thermal annealing of the defective systems has been performed at the thermostat temperature of 1400 K, corresponding to the typical experimental temperature for 3C-SiC deposition (in the case of ABOP potential, the temperature has been increased to 2000 K, in order to facilitate the dislocation glide motion).

Thermal dilation of the film has been accomplished scaling the box dimensions, where the scaling factor has been calculated for each potential simulating a 3C-SiC bulk cell in the NPT ensemble, using the Nose-Hoover barostat.

## *2.2. First principles calculations*

The calculations of the electronic structure have been performed by density-functional theory (DFT) with generalized-gradient (GGA) corrected exchange-correlation potentials [50], as implemented in the Quantum Espresso package [51]. Plane-wave basis set with a kinetic energy cutoff of 80 Ry have been used, with projector augmented wave (PAW) pseudopotentials [52], and a 1x4x1 Monkhorst-Pack grid for sampling the Brillouin zone of the 3C-SiC supercell, increased to 1x10x1 for the LDOS calculations. The structural relaxations have been performed until the average atomic force is lower than  $10^{-4}$  Ry/Bohr, using a conjugate gradient method and including van der Waals interactions within the semiempirical method of Grimme (DFT-D2) [53]. For the band structure and the LDOS calculations, meta-GGA exchange-correlation functionals have been exploited in order to improve the bandgap prediction of 3C-SiC. In particular, by using recently developed non-empirical strongly constrained and appropriately normed (SCAN) meta-GGA functionals [54] a bandgap of about 1.9 eV has been obtained as compared to 1.35 eV of the Perdew-Burke-Ernzerhof (PBE) GGA calculations. By comparing the PBE results and the meta-GGA ones, which are much closer to the experimental values, we understand the impact of the bandgap underestimation on the intra-gap states: the larger gap has mainly the effect of further separating the defect states from the conduction band (CB) minimum, but their position in energy with respect to the valence band (VB) is not much changed. Thus, we conclude that the

underestimation of the bandgap that one still has by using the SCAN functionals does not affect our prediction on the position of the intra-gap states with respect to the VB.

We modeled the partial dislocations by using periodic boundary conditions within a supercell approach. The super-cell is orthorhombic, with the three axis corresponding to the  $\langle -11-2 \rangle$ ,  $\langle 110 \rangle$  and  $\langle -111 \rangle$  directions of the 3C-SiC crystal, and it contains 1056 atoms, having sides of 58.64, 6.15 and 30.15 Å, respectively. Pairs of dislocation dipoles have been introduced in the supercells for the 90° and 30° partials, respectively, thus obtaining a supercell with both the Si- and C-core partial dislocations. For the termination of the double and triple SFs, the simulated supercells contain two dislocations dipoles at the opposite sides of the SFs (indicated as configuration A and B in subsection 3.2). The distance between the dislocation in dipoles (about 27 Å) has been verified to be large enough to rule out any relevant effects, caused by their interactions, on the predictions of the defect energy states, which are the main purpose of these first principle calculations.

### **3. Results and discussion**

The results are discussed in two following subsections. In the first one, a possible formation mechanism of dislocation complexes and multiple stacking faults is proposed and then corroborated by our MD simulations. In the second part, the *ab-initio* calculations of the electronic properties of the complexes obtained by the MD simulations are presented.

#### *3.1. Defect formation mechanism by molecular dynamics simulation*

##### *3.1.1 MD simulations of straight-line dislocations*

We exploited molecular dynamics simulations to reveal the key steps of the formation of dislocation complexes, which may be considered as candidates for the killer defects in 3C-SiC layers.

In zinc-blend crystals, which include also 3C-SiC, the primary slip system is  $\{111\} \langle 110 \rangle$ , i. e. the glissile dislocations nucleate and move in  $\{111\}$  planes, the dislocation lines are mainly directed along  $\langle 110 \rangle$  directions, and the deformations induced in the crystals are described by Burgers vectors  $\vec{b} = a/2 \langle 011 \rangle$ . A perfect glissile dislocation can dissociate in two partial dislocations with Burgers vectors  $\vec{b} = a/2 \langle 121 \rangle$  (Shockley dislocations) forming  $30^\circ$  and  $90^\circ$  angles with their respective dislocation lines, and a SF between the two cores.

In the early deposition stages of 3C-SiC layers on Si substrates, first a network of dislocations is formed in the SiC side of the 3C-SiC/Si interface, due to the high tensile misfit strain, and stress induced by it. The main part of the stress relaxation is provided by the direct formation of Lomer dislocations at the interface [26,27], i.e. sessile perfect dislocations not related to the stacking faults. Moreover, formation of glissile Shockley partial dislocations, which introduce SFs in the 3C-SiC layer may also contribute to the stress release [26,27]. Under tensile strain condition, the  $90^\circ$  partials lead the relaxation process and are driven towards the 3C-SiC/Si interface [27]. The residual strain can be further released during subsequent 3C-SiC layer deposition by the motion of the glissile dislocations, already present in the layer, or by the nucleation of new extended defects at the film surface, and propagation of them into the bulk.

Fig. 1 reports the MD simulations results for the simulation set A. A  $90^\circ$  partial dislocation was inserted deep in the simulation cell, the red color in Fig. 1 corresponding to the atoms forming the core of this dislocation and the orange to the

atoms belonging to the SF, respectively. Notice the compressive lobe above the core of the  $90^\circ$  partial, decreasing the initial tensile strain, shown in the volumetric strain maps in the insets of Fig. 1.

The dimension of the simulation cell along the direction of the vector  $\vec{s}$  has been chosen so that the array of  $90^\circ$  partial dislocations created by the periodic boundary condition in this direction would cause the slightly compressive in-plane strain ( $\sim 0.45\%$ ) present after the carbonization procedure, corresponding to the relationship of 5 SiC unit cells on 4 Si cells at the typical growth temperature. Under compressive strain condition,  $30^\circ$  partial dislocations lead the stress relaxation moving from the 3C-SiC surface toward the interface with Si substrate [55]. Therefore, to understand the formation process of dislocation complexes,  $30^\circ$  partial dislocations were also inserted in the simulation cell. In particular they are placed at a distance of 2.5 nm from the free surface of the 3C-SiC film, into the glide planes parallel to the one hosting the  $90^\circ$  dislocation.  $30^\circ$  partial dislocations are shown in Fig. 1 with their cores in green color. During MD simulated annealing (1400 K, 50 ps),  $30^\circ$  dislocation turns to be always expelled to the surface, as reported in the first row of Fig. 1, unless it is inserted in the plane just adjacent to the SF plane hosting the  $90^\circ$  dislocation, as demonstrated in the second row of this figure. In the latter case, the results of simulations show that the  $30^\circ$  partial is driven away from the 3C-SiC layer surface, while the  $90^\circ$  partial is pulled in the opposite direction (Fig. 1, second row). When the two cores of  $30^\circ$  and  $90^\circ$  partial dislocations are at the closest distance, a new defect is created terminating the double-plane SF. This new defect, known as  $30^\circ$  extrinsic partial dislocation, has been experimentally seen both in 3C-SiC as well as other compounds [56]. The observed dislocation dynamics is due to both the strain release process in the film and the attractive elastic interaction

between the two dislocations. The latter effect is demonstrated by the volumetric strain color maps presented in the second row of Fig. 1. Namely, decreasing the distance between the  $30^\circ$  and  $90^\circ$  dislocations, the color lobes corresponding to the strain of opposite signs increasingly overlap, with partial mutual cancellation. In the experimental case, the simulated mechanism of the formation of  $30^\circ$  extrinsic partial dislocation should be enhanced by the lower formation energy of double SF with respect to the single one, not accurately reproduced by the potential used for MD simulations.

Starting from the  $30^\circ$  extrinsic partial dislocation with a double stacking fault, we go on by inserting a second  $30^\circ$  partial dislocation, as illustrated in the third row of Fig. 1, where the core atoms are colored in fuchsia. This newly inserted dislocation has a screw component of the Burgers vector opposite to the one of already existing  $30^\circ$  partial. Therefore, we label this dislocation as  $-30^\circ$  in Fig. 1. The choice of this specific direction of the dislocation Burgers vector has two reasons. First, as  $30^\circ$  partial it releases the residual compressive strain as required by the system. Second, summed with the Burgers vector of already present  $30^\circ$  extrinsic partial, a zero total Burgers vector is resulted, which is the only possible case to form stable triple dislocation complexes, according to our recent findings [57]. Gliding of this dislocation with its SF extension is observed as a result of MD simulations only when it is inserted in the plane adjacent to the double SF. The new dislocation reaches the existing stable defect and forms with it a new defect configuration, which terminates triple SF, composed of three partial dislocations, having the total Burgers vector equal to zero. The motion of the  $-30^\circ$  dislocation does not change by inserting it adjacent to the SF formed by  $90^\circ$ , or  $30^\circ$  PD, only being slower in the latter case, due to a weaker driving force. Therefore, the defects with the second type of the

dislocation stacking are expected to be less probable to observe experimentally as compared to the first type in defect stacking. Interaction of the  $30^\circ$  partial dislocation with the  $30^\circ$  extrinsic partial dislocation to form a triple dislocation complex takes place according to the mechanism described above for the case of  $90^\circ$  and  $30^\circ$  partial interaction. We note also that the triple SF is equivalent to an inclusion of a hexagonal 6H-SiC stripe and is often defined as a microtwin. The triple dislocation complex terminating the twin inclusion corresponds to the one observed experimentally in phase transitions between 3C and 6H phases [58], as well as forming the  $\Sigma 3$  {112} incoherent twin boundaries [59,60,61] .

Modeling the dislocations as infinite straight segments, as discussed above, enabled us to fully capture their interaction along the direction parallel to the 3C-SiC/Si interface and to find possible configurations to be probed as killer defects. Their electronic properties are then discussed in Section 3.2. The results for full dislocation lines and closed loops, in addition, are presented in the next subsection to complete the general understanding of the dislocation dynamics in 3C-SiC/Si, and to create a link with experimental observations.

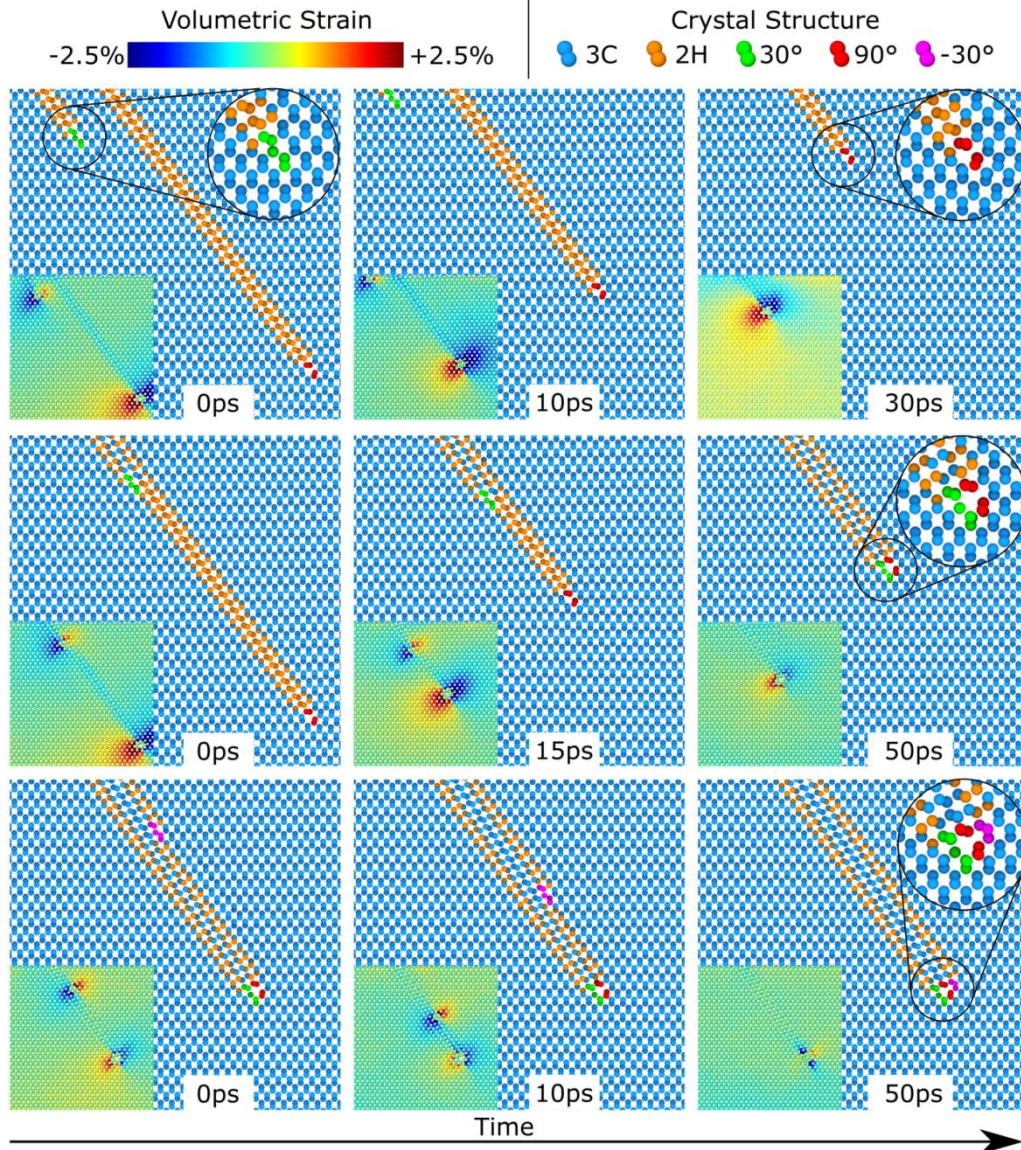


*Fig. 1. MD simulation snapshots of the proposed triple SFs and relative defect termination formation mechanism. First figure row: 30° partial dislocation (core atoms in green) is inserted six {111} planes far from the glide plane of a 90° partial glide plane (core atoms in red). Both dislocations are expelled. Second row: 30° partial dislocation is inserted in the adjacent plane of 90° glide plane. Dislocations move in opposite directions, join and form a 30° extrinsic partial dislocation. Third row: another 30° partial dislocation (core atoms in fuchsia) is inserted in the plane*

*adjacent of the double SF. It reaches the 30° extrinsic partial and forms the stable triple defect. In the insets volumetric strain maps for each snapshot are reported.*

### *3.1.2 MD simulation of 3D evolution of dislocation loops*

Three-dimensional shapes of stacking faults depend on several factors, such as local strain fields in the crystal, interaction with other defects, presence of free surfaces or interfaces, and characters of the stacking fault terminating dislocations. In this section, we shed light on the influence of the latter issue on both single plane and multiple plane SFs in 3C-SiC layers.

#### *3.1.2.1 Single SF loops*

As has been already mentioned above, partial dislocations in zinc-blend crystals have preferential line directions coinciding with equivalent  $\langle 110 \rangle$  directions. Stacking faults lay in  $\{111\}$  planes, therefore their terminating dislocations have six preferential equivalent  $\langle 110 \rangle$  line directions lying in each plane. As a consequence, the evolution of a general-case SF is suitable to study starting from a closed hexagonally shaped partial dislocation (HPD) loop formed by the dislocations with equivalent  $\langle 110 \rangle$  lines enclosing the stacking fault as shown in Fig. 2 a and f. In view of the crystal geometry and nonequivalence of the Si and C species making up the 3C-SiC lattice, each dislocation loop comprises three segments terminated by silicon and three other segments terminated by carbon atoms. Furthermore, the Burgers vector of the loop always forms an angle  $90^\circ$  with one Si- and one C-terminated dislocation segment and angles of  $30^\circ$  with the rest of the segments.

Panels a) and f) of Fig. 2 schematically show the structures of HPD loops located in different possible glide planes. In particular, panel a) corresponds to the

HPD loops in (1-1-1) and (1-11) glide planes, while panel f) represents the loop in the (111) and (11-1) planes, respectively. Those planes are not equivalent in 3C-SiC, because of the stacking order of Si and C monolayers along the {111} that is opposite, as shown in Fig. 2 panels k) and l). This implies that the terminating species of each dislocation segment is inverted for the two classes of loops. We notice that the panels a) and f) report the specific cases of the loops releasing the tensile strain at the initial stages of the 3C-SiC deposition process. A single suitable choice exists for the Burgers vector of the loop in order to relax such a strain, namely the one at which it forms an angle of  $90^\circ$  with the loop segment parallel to the 3C-SiC/Si(001) substrate interface.

Fig. 2 b)-e) and g)-j) show the sketches of the evolution of the two types of HPD loops discussed above, as a result of the initial tensile strain relaxation. The final shape of the stacking fault enclosed by the loop is determined by the relative velocities of the bounding partial dislocations. In 3C-SiC, the  $90^\circ$  PDs are faster than  $30^\circ$  PDs. Therefore the segments with the Burgers vector perpendicular to the line direction will advance, distorting the dislocation line and reshaping the loop into a diamond shape (Fig. 2 panel b) and g)). At this point the loop further expands and the terminating species of the SF plays a key role in the evolution. Experimentally, silicon terminating dislocations are known to be faster than carbon ones [62, 63, 64], so they will move faster, reaching the 3C-SiC/Si substrate interface or the free surface of the epitaxial layer in the cases a)-e) and f)-j), respectively. The opposite half of the loop expands slowly, and the SF acquires a triangular shape. Further evolution will continue with a triangular loop shape until the C terminating segments finally reach the free surface or 3C-SiC film/Si substrate interface, respectively.

The HPD loop evolution in a tensile strained 3C-SiC crystal has been studied by classical molecular dynamics simulations to confirm the simple scheme described in the previous lines using simulation set B (see Section 2).

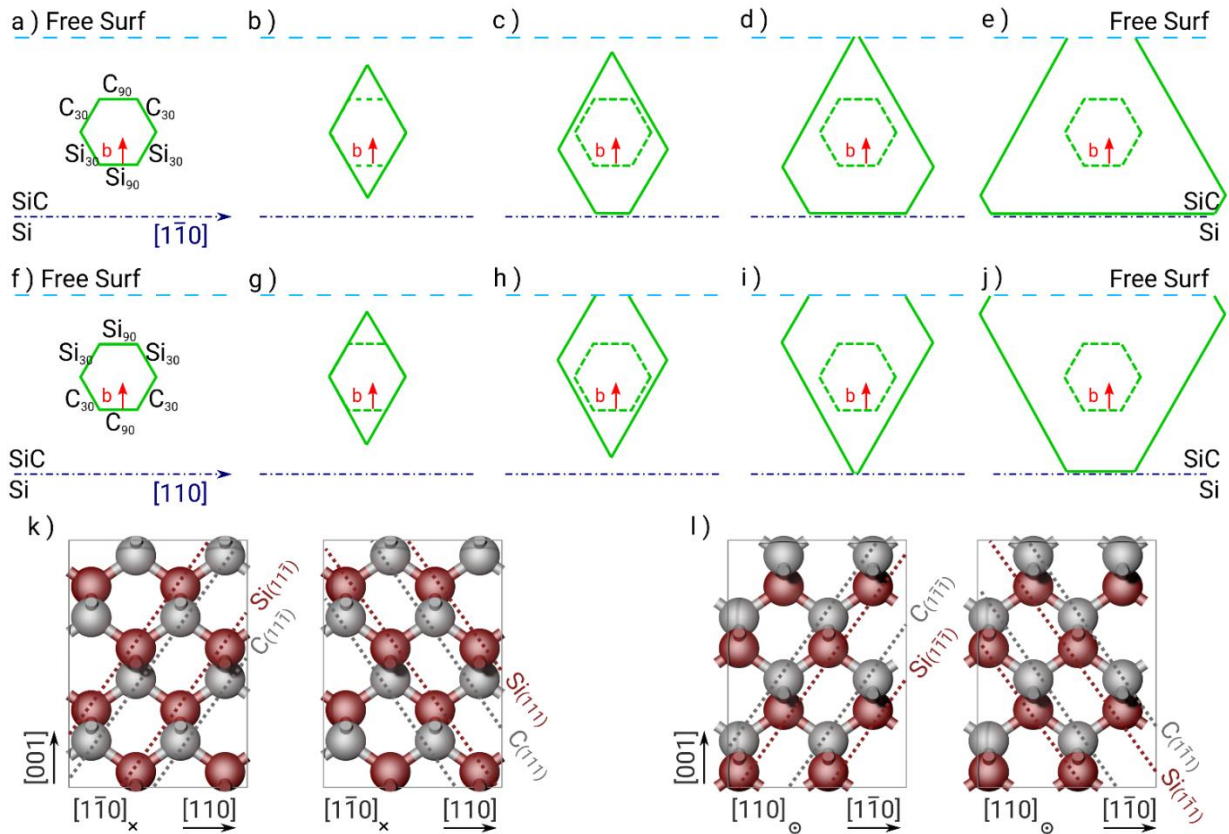


Fig. 2. Diagram of the evolution of HPD loops in different glide planes. The loop evolution is shown when the Burgers vector is  $\langle 112 \rangle$  in type and under tensile strain conditions. Burgers vectors are displayed as red arrows (the loop dislocation line direction can be either clockwise or anti-clockwise depending on the specific glide plane). Top row (a - e) shows the evolution of loops in  $(1\bar{1}\bar{1})$  and  $(1\bar{1}1)$  glide planes (i.e. the glide planes parallel to the  $[110]$  direction). In the middle row (f - j) the evolution of loops in  $(111)$  and  $(11\bar{1})$  glide planes (i.e. the glide planes parallel to the  $[1\bar{1}0]$  direction) is presented. Bottom row (k - l) provides the reference zinc-blend

structure projected in  $[110]$  and  $[1\bar{1}0]$  directions, relevant glide planes are highlighted by dashed lines.

Fig. 3 shows the results of the MD simulations of two HPD loops evolving under an external applied biaxial tensile strain ( $\epsilon_{xx} = \epsilon_{yy} = 4\%$ , this value is chosen arbitrarily, allowing a reasonable time scale for the observation of the HPD loop evolution). These simulations are identical except for the glide plane where the HPD loop is located. Under identical conditions of temperature (1400 K) and strain, the two loops evolve in full accordance with the sketches described above (see Fig. 2). It is evident from panel d) of Fig. 3 that the correlation between the final shape of the loop and its glide plane does correspond to the one explained before, and illustrated in Fig. 2.

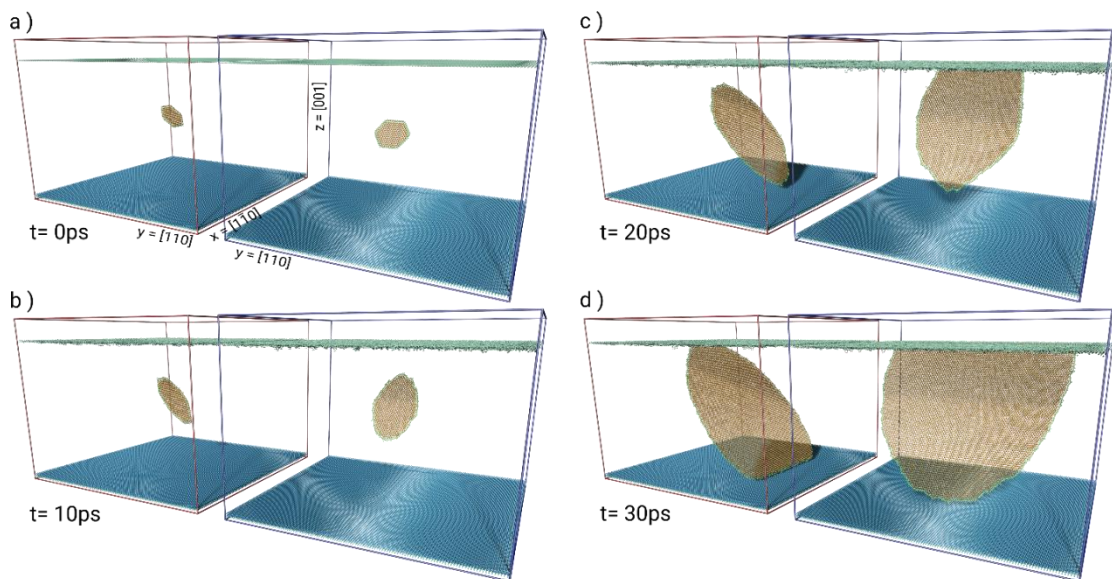


Fig. 3. Classical molecular dynamics simulations snapshots of the evolution of HPD loops. Two parallel simulations are shown: on the left (red cell) the evolution of an HPD loop that lays in the  $(111)$  plane is shown. On the right (blue cell) the evolution of an HPD loop laying in a  $(1\bar{1}\bar{1})$  plane is shown. Only stacking faulted atoms

(orange), fixed atoms (dark blue) and surface atoms (light blue) are shown for clarity. Three snapshots are reported: Initial configurations (a), and atomic configurations after 20 ps (b) and 30 ps (c).

### 3.1.2.2 Triple SF loops

In the simulations reported above, we limited our discussion to single plane SFs. However, the most common stacking faults are composed of three consecutive SF planes, forming twin regions [39]. In this section, we suggest the mechanism of twin formation based on the results presented in the previous sections. Using MD simulations, we analyze the three-dimensional equilibrium shape of the twin region, together with its boundary structure.

As previously described, the tendency to reduce tensile strain during early deposition stage of 3C-SiC layers is the driving force for the expansion of the SF and the displacement of its boundaries with partial dislocations. The orientation of the glide plane determines the orientation of the trapezoidal planar shape of the whole defect, as depicted in Fig. 2. At the subsequent 3C-SiC deposition stage, an inversion in the sign of the strain occurs, and the nucleation of defects with different Burgers vectors can take place. Referring to the results of MD simulations described in Section 2, one may state that the loops or semi-loops with Burgers vectors corresponding to the  $30^\circ$  PD lines parallel to the 3C-SiC/Si substrate interface should have a lower nucleation barrier in the planes adjacent to the existing SF plane. Attractive interaction between the dislocation segments of the stacking faults lying in neighboring glide planes contributes to the coordinated evolution shape of the SF by segment motion. As a consequence, a superposition of all three loops and a formation of a unique defect complex with total Burgers vector equal to zero can be

reasonably supposed. Note that it has also recently reported in [57] that the combination of three PDs corresponding to  $\vec{b}_{tot} = 0$  is the only stable defect terminating triple SF, any other PD combination results in the separation of bounding dislocations. The outcome of the process described here would lead to the stacking fault shapes proposed by Nagasawa in [65].

Unfortunately, MD simulations of the entire process of the formation of twin defect by superposition of stacking faults cannot be performed efficiently. The condition of low compressive strain corresponding to the experimental one at the later stage of the 3C-SiC deposition (around 0.45 %), would mean extremely long 30° HPD loop expansion leading to unachievably long computations. With respect to this, we performed simulations starting from entire superposition of the three partial dislocation loops and looking for the equilibrium configurations of the defects with  $\vec{b}_{tot} = 0$  along all the boundary segments. In particular, the energy has been minimized applying the conjugated gradient algorithm. The simulation results are presented in Fig. 4, in which the triple SF belonging to (111) (or, equivalently, to  $(1\bar{1}\bar{1})$ ) plane is shown in the upper panel, and the one located in the  $(1\bar{1}1)$  (or, equivalently,  $(1\bar{1}\bar{1})$ ) plane in the bottom panel, respectively. The core structures of each dislocation segment forming the triple defect are additionally shown in the inset circles, viewed in the cross-section perpendicular to the dislocation line directions. The core atoms are colored following the definitions of Fig. 1, namely red color corresponds to the atoms in the core of the dislocation loop nucleated first (for tensile strain relaxation at the early stage of 3C-SiC deposition), with a 90° PD parallel to the 3C-SiC interface. Fuchsia and green colors are used to mark the core atoms of the HPD loops nucleated thereafter for compressive strain relaxation. They have the 30° PDs parallel to the 3C-SiC interface. It is evident that, following the

triple SF loop boundary the core of the terminating defect changes (still keeping  $\vec{b}_{tot} = 0$ ) due to the change of the order of the composing partial dislocations.

Notice that the evolution of the loop segments parallel to the 3C-SiC interface is driven mainly by the strain relaxation process that, as shown in Section 3.1.1, causes the subsequent dislocation nucleation and migration towards the interface. The whole epitaxial layer tends to strain relaxation. We can suppose therefore that the described evolution of the misfit segments is significant for all the dislocation loops in the system under consideration. Behavior of the threading segments is more complex and less predictable. The interaction between the threading segments has been supposed as a main driving force of the motion. However, any local interaction between other defects can cause deviation from the described behavior. For this reason, we focus on the triple dislocation complexes created by the parallel to the 3C-SiC/Si substrate interface  $30^\circ$ - $90^\circ$ - $30^\circ$  partial dislocation sequences and study their electronic properties by ab initio calculations.

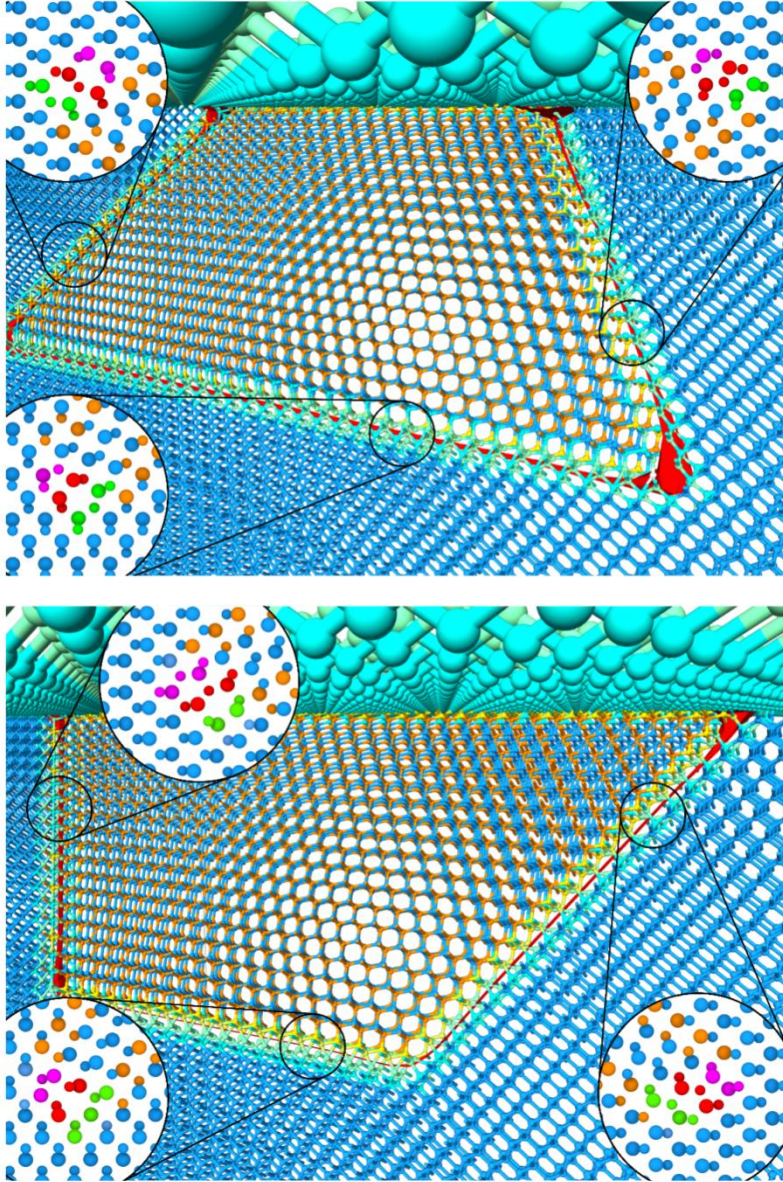


Fig. 4. Shape and terminations of a triple SF. Top: Shape of triple SF belonging to  $(111)$  or  $(1\bar{1}\bar{1})$  plane; Bottom: Shape of triple SF belonging to  $(\bar{1}\bar{1}1)$  or  $(\bar{1}\bar{1}\bar{1})$  plane. The defect line is colored in red. In the circles the core structures viewed in the cross sections perpendicular to the line directions are shown. Core atoms are colored to indicate the Burgers vector of the dislocation lying in that plane, with the same nomenclature of Fig. 1. Blue sticks and atoms correspond to zinc-blend structure, orange ones to wurzite structure. Lighter hues are used to indicate the defect surroundings.

### 3.2. *Electronic properties by ab-initio calculations*

The changes in the electronic properties caused by the presence of SFs in 3C-SiC have been investigated by different theoretical groups [37,38,66,67] and there is a general consensus that SFs in 3C-SiC do not give rise to electrical active states in the fundamental bandgap of the material, in contrast to the hexagonal SiC phases. As highlighted above, SFs in 3C-SiC correspond to the inclusions of stripes with hexagonal structure in the cubic phase. The valence band edges of the cubic and hexagonal polytypes are almost aligned [68], and the difference in the bandgap values between the cubic and the hexagonal phases causes a band-offset mostly between their conduction bands. In particular, the 3C phase has the smallest bandgap as compared to the hexagonal polytypes, thus the inclusion of hexagonal stripes (i.e. SFs) in 3C-SiC creates quantum barriers as evident in Fig. 5, where the local density of states (LDOS) obtained by density functional theory (DFT) calculations has been plotted as a function of the position along the c-axis ([111] direction) of a simulated 3C-SiC supercell, which includes a triple SF (the behavior with single and double SFs is identical). This is a distinctive aspect of the SFs in 3C-SiC, as compared to the hexagonal polytypes and particularly 4H-SiC, where a quantum well-like behavior of the SFs has been found [37], causing the rise of active unoccupied states in the SiC bandgap. On the contrary, SFs in 3C-SiC do not give rise to intra-gap states, which have been inferred as a very likely cause of the leakage current in 3C-SiC devices. However, SFs have finite dimensions in real crystals and their terminations have not yet been included in the analysis of the electronic properties of defective 3C-SiC.

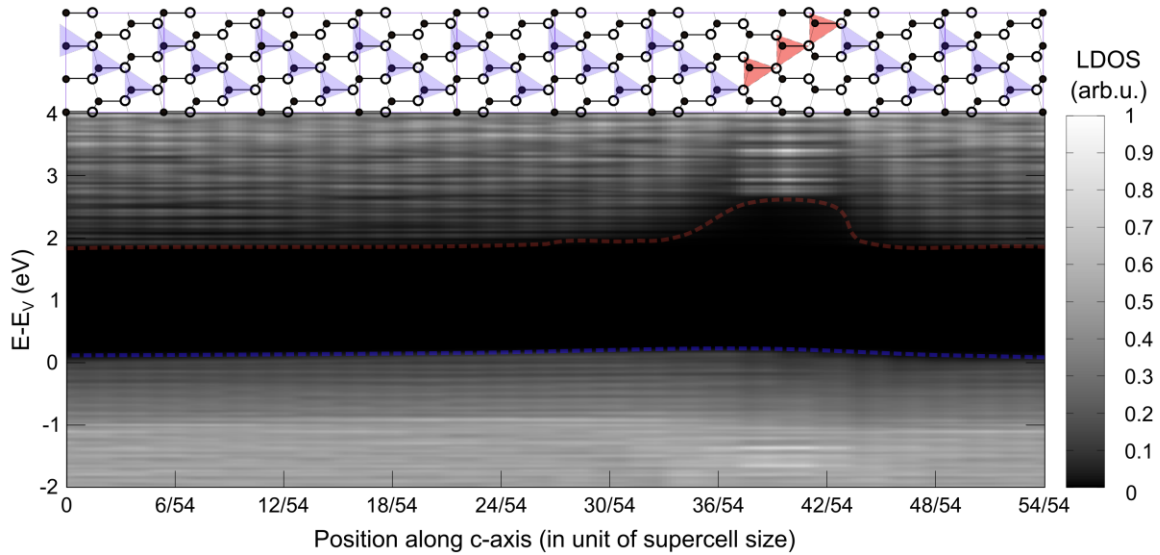
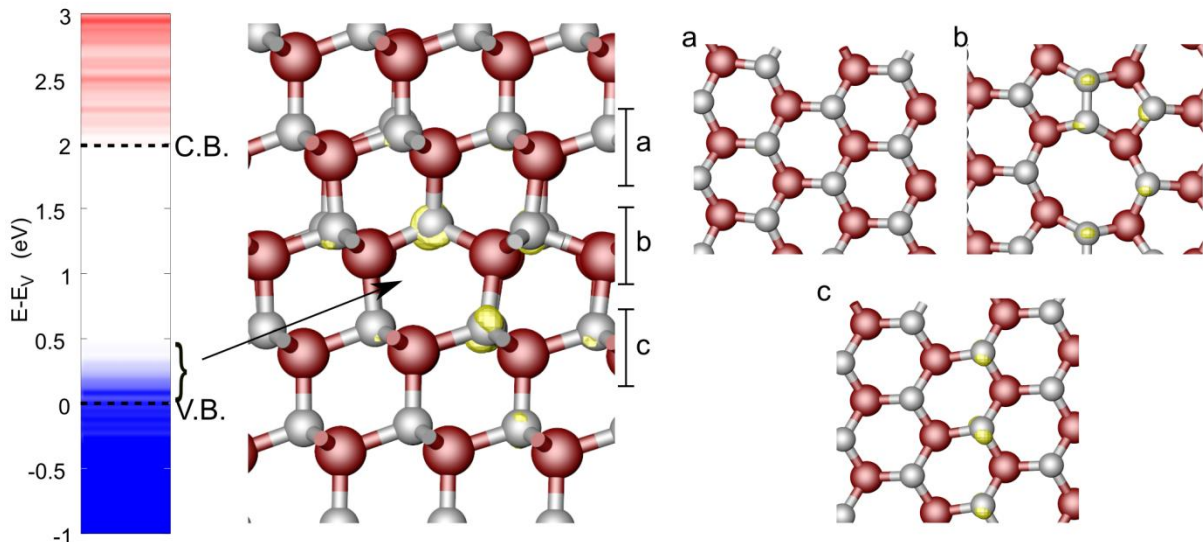


Fig. 5. Local density of states (LDOS) integrated in slice boxes along the  $c$ -axis of the simulated supercell, which is illustrated on top. The red triangles highlight the tetrahedra of the faulted planes as compared to the perfect stacking of the 3C-SiC (blue tetrahedra). The dotted lines highlight the trend of the band edges along the  $c$ -axis: a quantum barrier is very evident in the space region where the triple SF is present.

### 3.2.1 Terminating single SF by partial dislocations

Atomistic details of the core dislocations may have a crucial impact on the electronic properties of the material. By exploiting the structures obtained after the MD, we investigated by means of DFT calculations different possible atomistic configurations for the partial dislocations terminating the single, double and triple SFs with two main goals: finding the most thermodynamically stable configurations and among them identifying those detrimental to the electronic properties of the devices. Between all possible configurations, we focus on those that do not have Si or C dangling bonds. In fact, Bernardini *et al.* [66] found for the (single)  $30^\circ$  partial dislocations in SiC that *unreconstructed* geometry for both Si- and C-core partials,

showing Si or C dangling bonds, are energetically unfavored, as compared to the *reconstructed* case. The latter shows Si-Si or C-C covalent bonds, which saturate the dangling bonds of the *unreconstructed* geometry, pushing the defect states outside the bandgap or close to valence band edge in case of Si-core 30° partial dislocations. In particular, the strong C-C bonds of the C-core of the 30° partial dislocations enhance the energy separation between bonding and anti-bonding states associated with the hybridization of their orbitals, resembling the  $sp^3$  hybridization in bulk SiC and thus preventing the formation of intra-gap states, as evident in Fig. 6. On the contrary, the Si-Si bonds of the Si-core of the 30° partial dislocations, illustrated in Fig. 7, is much weaker than the C-Si bonds in the pristine SiC. As matter of the fact, the energy separation between bonding and anti-bonding states of the Si-core atoms is not as large as in the pristine SiC case, and intra-gap states are visibly formed close to the VB edge (see Fig.7).



*Fig. 6. Defect states at the C-core of the 30° partial dislocation: the Kohn-Sham eigenvalue spectra of the dislocations core are plotted in the left side, with the blue (red) lines indicating unoccupied (occupied) states and the two dashed lines*

indicating the valence band (VB) and the conduction band (CB) edges in the pristine SiC. The side view of the dislocation core with the charge density of the corresponding gap states is also illustrated, including the top view of the (-111) glide planes (as in the side view with a, b and c labels) and the charge density of the gap states. Red and gray balls indicate Si and C atoms, respectively.

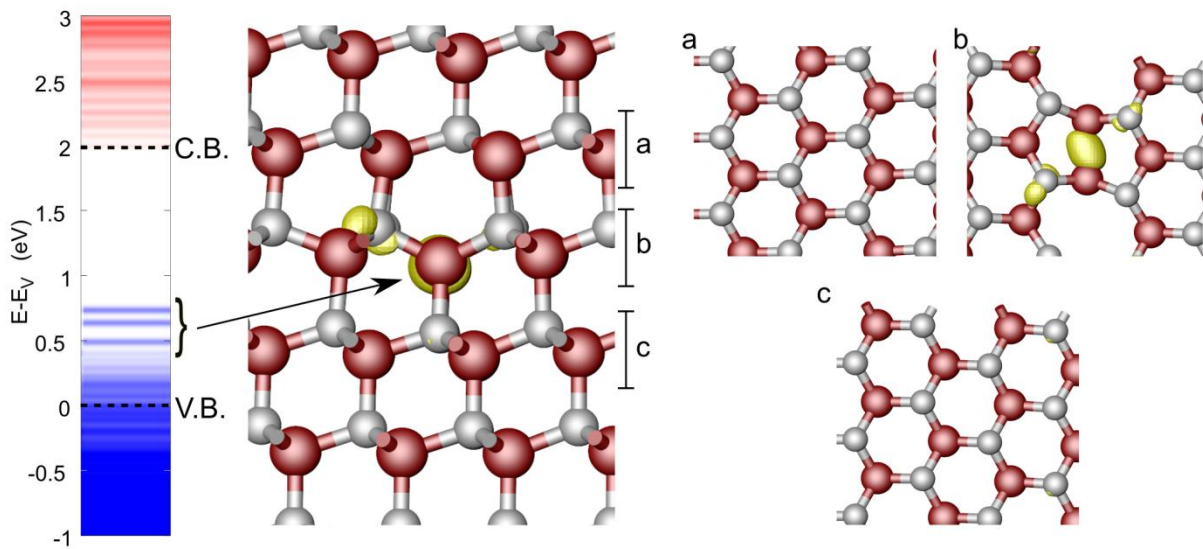
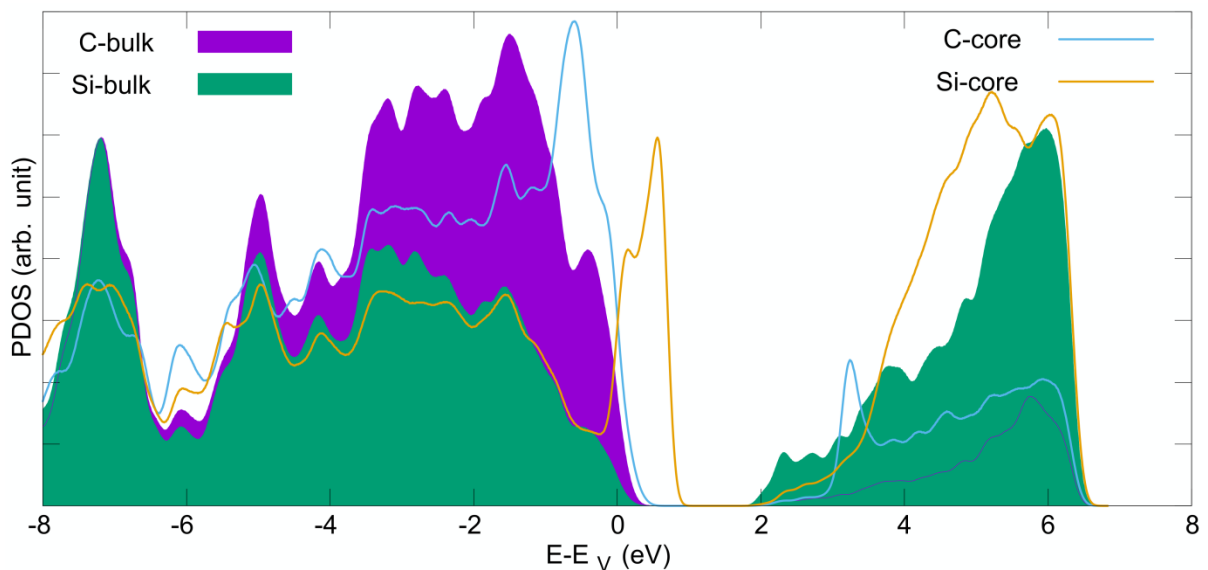


Fig. 7. Defect states at the Si-core of the  $30^\circ$  partial dislocation: the Kohn-Sham eigenvalue spectra of the dislocations core are plotted in the left side, with the blue (red) lines indicating unoccupied (occupied) states and the two dashed lines indicating VB and CB band edges in the pristine SiC. The side view of the dislocation core with the charge density of the corresponding gap states is also illustrated, including the top view of the (-111) glide planes (as in the side view with a, b and c labels) and the charge density of the gap states. Red and gray balls indicate Si and C atoms, respectively.

The partial density of states (PDOS) associated with C and Si atoms at the core of the partial dislocation or in the pristine bulk, as plotted in Fig. 8, better

clarifies these aspects. The VB of the 3C-SiC is mainly originated by orbitals of the C-atoms, while the Si atoms contribute more to the CB states. When C-C (or Si-Si) bonds are present in SiC, the gap between bonding and anti-bonding states is due to the hybridization between orbitals of the same atomic type, which then contribute both to the formation of the CB and VB. In fact, the PODS of the C-core atoms plotted in Fig. 8 shows a marked peak in the CB, which is not present in the PDOS of C-bulk atoms, but this peak is well above the CB edge. The Si-core atoms induce a PDOS peak in the VB, also not present in the bulk case. This peak evidences states that are above the VB edge, reasonably due to the weaker Si-Si bonds, as compared to the C-Si ones, and forming band-like states from the VB edge up to about 0.7 eV above the VB. The band-like behavior of these states will be discussed further below.



*Fig. 8. Partial density of states (PDOS) of 3C-SiC containing both a Si- and a C-core 30° partial dislocations. The PDOS of C and Si atoms in the core of the dislocation is compared to that of C and Si atoms in the pristine region of the bulk SiC.*

The electronic properties of the 90° partial dislocations illustrated in Fig. 9 and

10 are very similar to the cases of the 30° partial dislocations, and only the Si-core 90° partial dislocations (Fig. 9) show intra-gap states, but not the C-core ones (Fig. 10). These intra-gap states generated by the Si-Si bonds of the 90° partial dislocation are even higher in energy and thus closer to the CB, as compared to the states due to the Si-core 30° partial dislocations, because of the longer Si-Si bonds in the 90° partials. The weaker Si-Si bonds are responsible for the smaller gap between these states and the CB states, in agreement with the description drawn above.

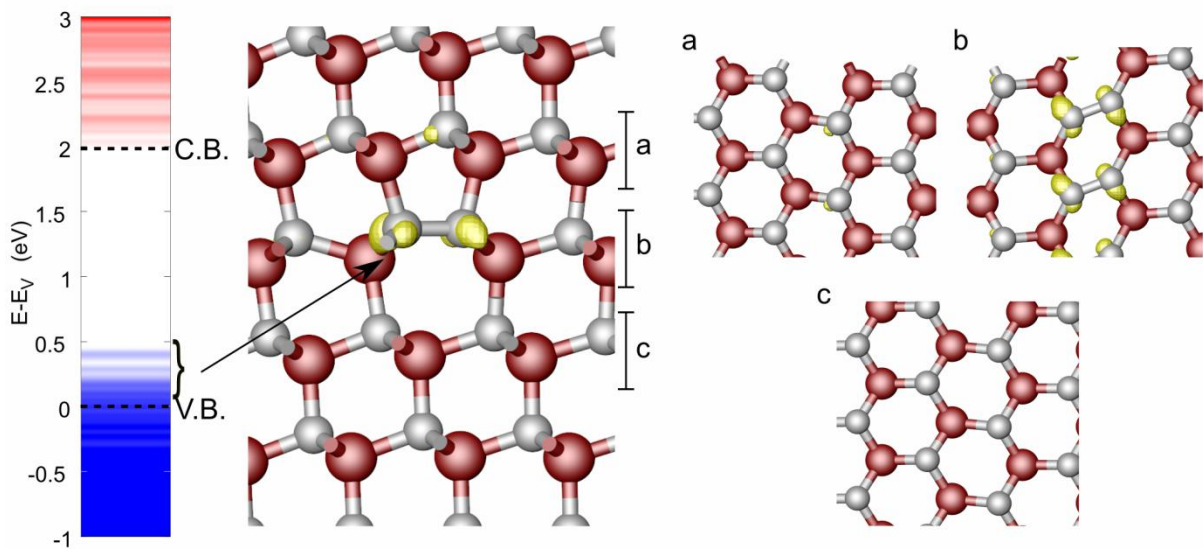


*Fig. 9. Defect states at the C-core of the 90° partial dislocation: the Kohn-Sham eigenvalue spectra of the dislocations core are plotted in the left side, with the blue (red) lines indicating unoccupied (occupied) states and the two dashed lines indicating VB and CB edges in the pristine SiC. The side view of the dislocation core with the charge density of the corresponding gap states is also illustrated, including the top view of the (-111) glide planes (as in the side view with a, b and c labels) and the charge density of the gap states. Red and gray balls indicate Si and C atoms, respectively.*

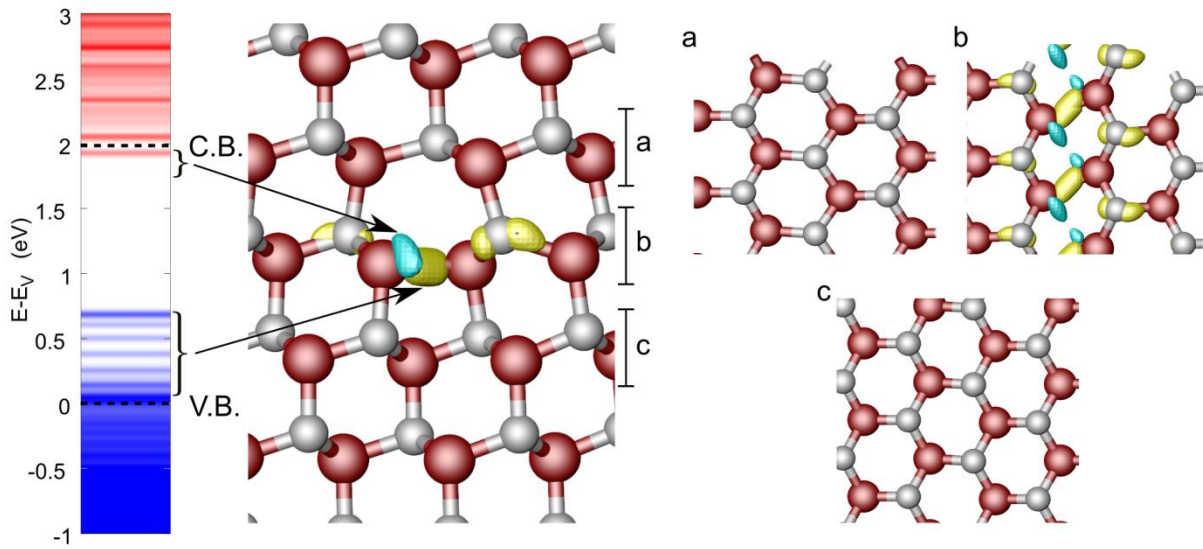


Fig. 10. Defect states at the Si-core of the  $90^\circ$  partial dislocation: the Kohn-Sham eigenvalue spectra of the dislocations core are plotted in the left side, with the blue (red) lines indicating unoccupied (occupied) states and the two dashed lines indicating VB and CB edges in the pristine SiC. The side view of the dislocation core with the charge density of the corresponding gap states is also illustrated, including the top view of the  $(-111)$  glide planes (as in the side view with a, b and c labels) and the charge density of the gap states. Red and gray balls indicate Si and C atoms, respectively. The different colors of the charge density highlight the different integration energy ranges.

### 3.2.2 Double SF

The results on the electronic properties of the partial dislocations terminating the single SF in 3C-SiC evidence the potential impact of these defects on the electronic properties of 3C-SiC. Still, the intra-gap states due to the Si-core partial dislocations are found at energies about 1.5 eV lower than the CB, minimum, probably too far in energy from the conduction band to be the only cause of trapping-assisted recombination/tunneling processes [20,68], which have been

related to the high leakage current experimentally observed in 3C-SiC devices. However, we have shown in a different work [7] how double and triple SFs are markedly more stable than the single ones. The MD simulations have also shown how the termination of the double and triple SFs are central in the formation mechanisms and evolution of dislocations (see Fig. 1), and they have highlighted the structural complexity of these dislocations, which could induce electronic defect states even worse than those found for the dislocations terminating the single SFs.

We found two main stable structures for the dislocations terminating the double SFs and they are illustrated in Fig. 11 and 12. They are basically composed of a 30° partial on top of a 90° partial: the structure “A” illustrated in Fig. 11 is composed of a C-core 30° partial (see inset a) on top of a Si-core 90° partial (see inset b), while the structure “B” (Fig. 12) shows a Si-core 30° partial (see inset a) on top of a C-core 90° partial (see inset b). The band structure corresponding to the configuration A does not evidence particular intra-gap states, still there are few states that vary similarly to those found for the simple Si-core 90° partial. Indeed, also in this case the Si-Si bond of the 90° partial dislocation causes the deepest defect states, as evidenced in the charge density plot of Fig. 11. On the contrary, nothing is found in the gap as due to the C-C bond of the 30° partial dislocation, in agreement with results found for the dislocations terminating the single SF.

The configuration B does show evident deep defect states, mostly due to the Si-core 30° partial dislocations, and extending much higher in energy as compared to the Si-core dislocations terminating the single SF. Indeed, the charge density plots show that the Si-core 30° partial dislocations are responsible for a dispersive band lying in the SiC bandgap, approximately from 0.7 eV to 1.1 eV above the VB edge. Although the C-core 90° partial dislocation does not contribute directly to these

states, as evidenced by the charge density plot, the C atoms of the dislocation core are bonded to the Si atoms of the Si-core  $30^\circ$  partial dislocation lying above. Because of the stronger C-C bonds as compared to the Si-C bonds, the hybridization of the Si-core atoms (which are themselves bonded to another Si atom, two bulk-like C and one C-core atoms) gets even weaker, with the bonding and anti-bonding states having a smaller gap as compared to the single Si-core  $30^\circ$  partial dislocation. This is likely the main reason for the up-shift of the intra-gap states.

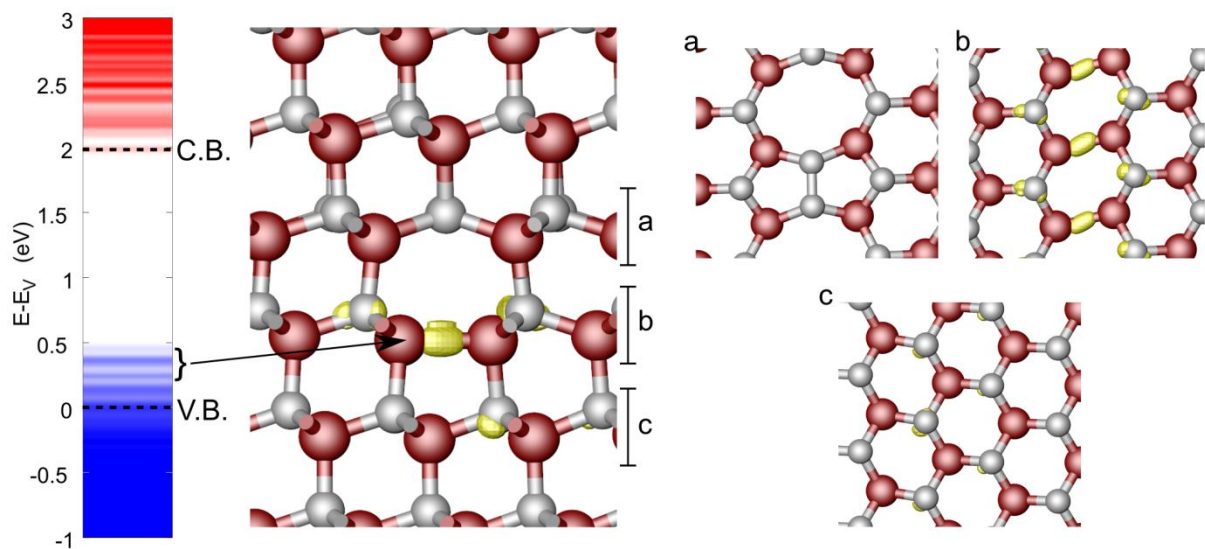


*Fig. 11. Defect states at the double dislocation complex (configuration A): the Kohn-Sham eigenvalue spectra of the dislocations core are plotted in the left side, with the blue (red) lines indicating unoccupied (occupied) states and the two dashed lines indicating VB and CB edges in the pristine SiC. The side view of the dislocation core is illustrated and the corresponding top view of the (-111) glide planes are shown in the insets a, b and c. Red and gray balls indicate Si and C atoms, respectively.*

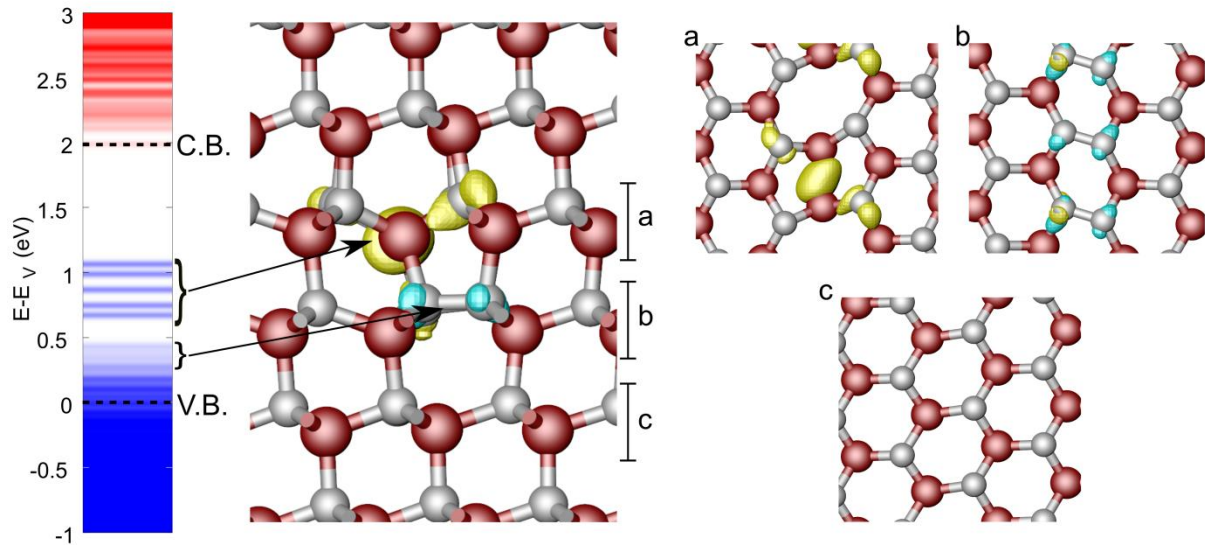


*Fig. 12. Defect states at the double dislocation complex (configuration B): the Kohn-Sham eigenvalue spectra of the dislocations core are plotted in the left side, with the blue (red) lines indicating unoccupied (occupied) states and the two dashed lines indicating VB and CB edges in the pristine SiC. The side view of the dislocation core with the charge density of the corresponding gap states is also illustrated, including the top view of the (-111) glide planes (as in the side view with a, b and c labels) and the charge density of the gap states. Red and gray balls indicate Si and C atoms, respectively. The different colors of the charge density highlight the different integration energy ranges.*

### 3.2.3 Triple SF

For the triple dislocation complex, we investigate some candidate structural configurations after the MD simulations and we show the two most stable ones in Fig. 13 and 14. In analogy with the double SF case discussed above, these defects are composed of the stacking of three partial dislocations, two of them (top and bottom ones) are  $30^\circ$  and have the same core species (e.g. C-core for configuration A, while Si-core for configuration B), while the intermediate one has  $90^\circ$  character and has

the different core species (e.g. Si-core for the configuration A, C-core for the configuration B).

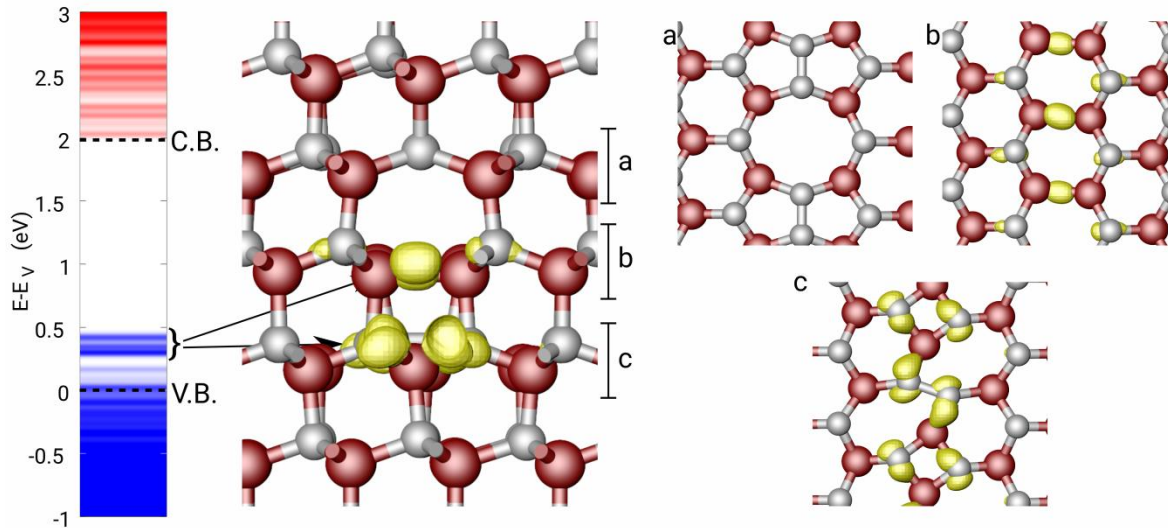


*Fig. 13. Defect states at the triple dislocation complex (configuration A): the Kohn-Sham eigenvalue spectra of the dislocations core are plotted in the left side, with the blue (red) lines indicating unoccupied (occupied) states and the two dashed lines indicating VB and CB edges in the pristine SiC. The side view of the dislocation core with the charge density of the corresponding gap states is also illustrated, including the top view of the (-111) glide planes (as in the side view with a, b and c labels) and the charge density of the gap states. Red and gray balls indicate Si and C atoms, respectively.*

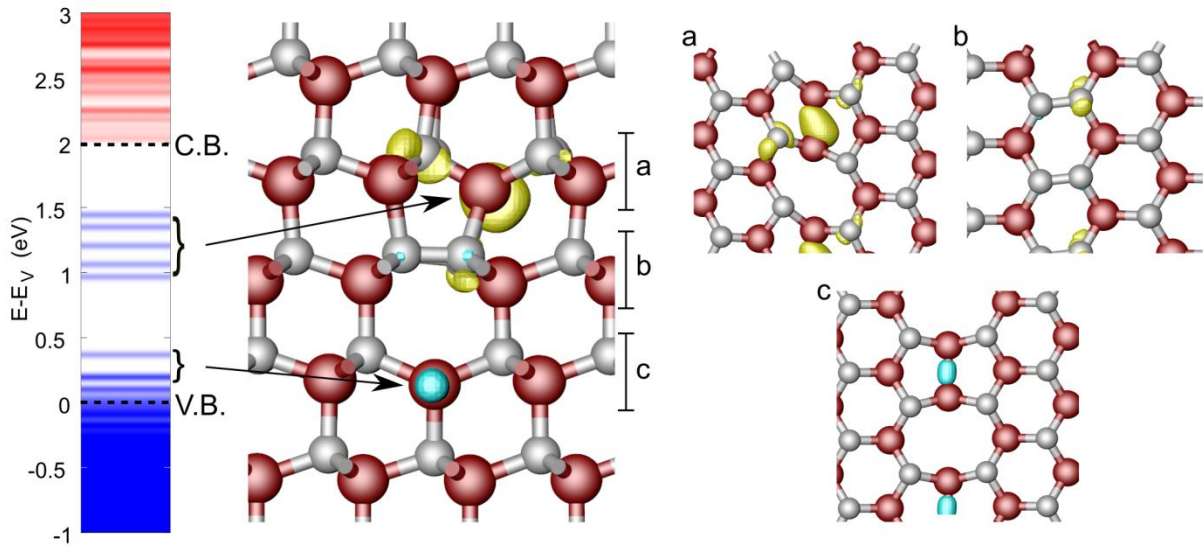
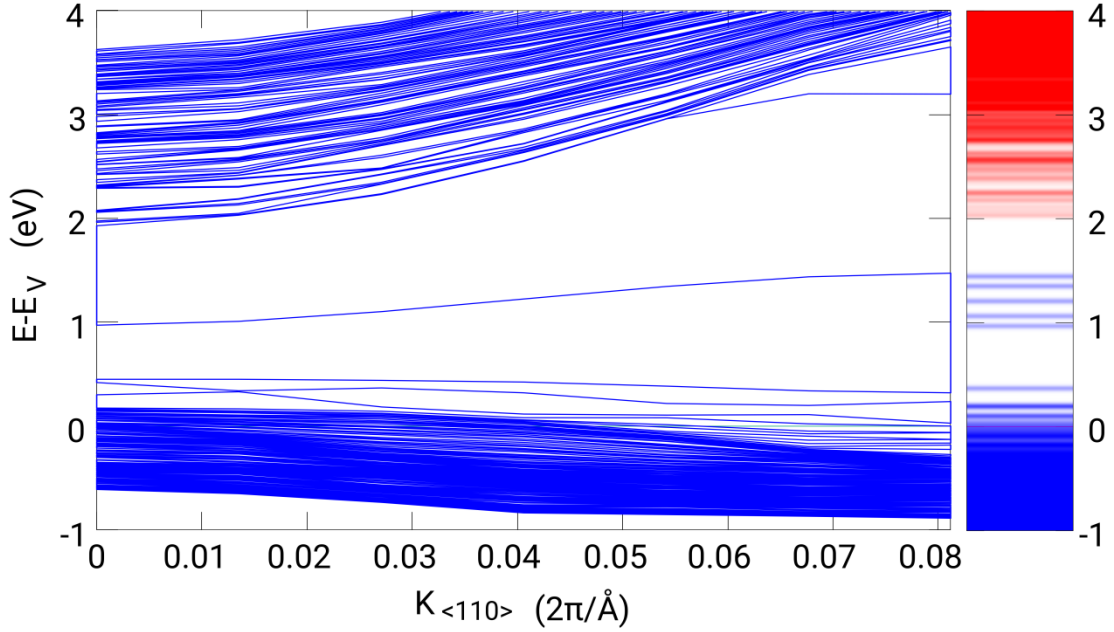


Fig. 14. Defect states at the triple dislocation complex (configuration B): the Kohn-Sham eigenvalue spectra of the dislocations core are plotted in the left side, with the blue (red) lines indicating unoccupied (occupied) states and the two dashed lines indicating VB and CB edges in the pristine SiC. The side view of the dislocation core with the charge density of the corresponding gap states is also illustrated, including the top view of the (-111) glide planes (as in the side view with a, b and c labels) and the charge density of the gap states. Red and gray balls indicate Si and C atoms, respectively.

In fact, we find that two dislocations of the configuration A (illustrated in the inset (a) and (b) in Fig. 13) are very similar to the single  $30^\circ$  C- and  $90^\circ$  Si-core partials, thus their defective states are outside the gap (C-core) or close to the valence band-edge (Si-core), very similarly to the configuration A of the double SF discussed above. But this triple SF termination has, in addition, another single  $30^\circ$  C-core partial (see inset (c) in Fig. 13), which although showing a slightly different reconstruction than the top one, has defect states laying still in the same energy range (below 0.5 eV from the VB), as originating from the bonds of the C-core atoms.

On the contrary, Fig. 14 evidences that the configuration B, having two 30° Si-core partials and a 90° C-core one in between them, is more problematic in terms of defect energy states. In fact, similar to the double SF case, the (top) 30° Si-core partial is responsible for a dispersive band lying in the SiC bandgap from about 1.0 eV to about 1.5 eV above the VB edge (see inset (a) in Fig. 14). As compared to the termination of the double SF (configuration B), the defect energy band of this defect is almost identical, but shifted upward by about 0.4 eV. This shift is mainly due to the different Si-Si bond length of the 30° Si-core partials: the termination of the double SF has a Si-Si bond length of about 2.33 Å as compared to 2.39 Å of the top 30° Si-core partial in the termination of the triple SF. The larger bond length of the 30° Si-core partial in the triple SF, originating from the particular stacking geometry of the three partials, leads to even weaker bonds as compared to the Si-Si bonds in the double termination, thus reducing further the gap between bonding and anti-bonding states. While the top 30° Si-core partial introduces these deep states in the 3C-SiC gap, the bottom one has states closer to the VB (see inset (c) in Fig. 14), and very similar to those of the single 30° Si-core partial dislocation. These is due to the fact that the Si atoms of the top partial are bonded to the C-core atoms of the 90° middle partial, as in the case of the termination of the double SF, while the bottom 30° Si-core partial is in the simple configuration as the single 30° partial, but just having slightly shorter Si-Si bond length (2.36 Å as compared to 2.37 Å of the single one).



*Fig. 15. Band structure along the  $\langle 110 \rangle$  direction for the supercell containing the terminations of the triple SF. The deep defect states in the LDOS are clearly due to a single dispersive band.*

Finally, in Fig. 15 the band structure along the  $\langle 110 \rangle$  direction for the supercell containing the triple SF and the terminations of Fig. 13 and Fig. 14 is plotted. One can clearly see that the 5 energy levels appearing in Fig. 12 and Fig. 14 and forming the defect energy bands at 0.6-1.1 eV and 1.0-1.5 eV, respectively, are not different energy states, but a single dispersive branch, originating from the periodicity of the defect along the dislocation line. The discrete energy levels in Fig. 12 and Fig. 14 are then an artifact of the limited K-points employed for the calculation of the LDOS.

Thus, we conclude that the most plausible candidates as killer defects in 3C-SiC are the partials terminating the double and triple SFs illustrated in Fig. 12 and Fig. 14, where the particular configuration of the Si-core  $30^\circ$  partials pushes the states of the

covalent bonding of the Si-core inside the gap of the pristine SiC. Because of the periodicity of the defect along the dislocation line, these defects states are also dispersive in the k-space, thus forming 0.5 eV wide defect bands in the gap of the pristine SiC, while shallow defects are expected for the termination of the single SF. Note also that the triple dislocation complex is structurally identical to the complexes forming the  $\Sigma 3$  {112} incoherent twin boundaries [59,60,61] which are then expected to lead to very similar electronic defect states. Experiments clearly show the coexistence of double and triple SFs in 3C-SiC, with preference of the latter, together with a minor occurrence of the single SFs [39]. From our results we can conclude therefore that the whole defect population is likely responsible for intra-gap states filling the gap of 3C-SiC up to about 1.5 eV from the VB maximum.

#### **4. Conclusions**

In this paper we have presented an in-depth theoretical/computational analysis of the most typical extended defects in 3C-SiC/Si(001).

Large-scale MD simulations based on the classical Vashista potential [41] were exploited to investigate the physical origin of defect complexes typically observed in experiments. In particular, we have shown that partial dislocation complexes terminating triple SFs can be easily generated during dislocation dynamics, under the compressive strain conditions which follow the formation of sessile dislocation arrays at the 3C-SiC/Si interface. Configurations revealed by MD simulations were subsequently analyzed and re-converged by DFT calculations. This multiscale approach was precious in saving computational time: by using DFT only, the computational cost would have precluded the exploration of defect dynamics on any meaningful time scale.

After completing the structural analysis, we have investigated the influence of the defects on the electronic properties of 3C-SiC. Meta-GGA exchange-correlation functionals have been exploited in order to improve the bandgap prediction. It turned out that the net result of a distribution of defects including single, double, and triple SF is a significant filling of the gap, with detrimental consequences in terms of leakage currents. As defect states induced by the partial dislocation terminating the single SF are observed to lay close to the edge of the valence band, we conclude that dislocation complexes, terminating double and triple SF, are killer defects in 3C-SiC.

Based on these findings, a next important step in the development of high-quality epitaxial 3C-SiC would involve lowering the concentration of partial dislocation complexes. Further experimental and theoretical research is surely needed in order to find optimal growth conditions for achieving such a result.

We notice that the usual solution (for several different systems) in epitaxy of raising the temperature to lower the defect density might not work in this case. In a recent paper [7], indeed, we showed that thermodynamics favors hexagonal SiC vs 3C-SiC only above a critical high temperature. As multiple SF correspond to insertion of hexagonal phases within the cubic one, raising temperatures too much might be counterproductive. As an alternative, to reducing the effect of dislocation complexes, one could aim at tailoring their core, and push the intra-gap defect states out of the gap. Controlled insertion of contaminants could help in this respect.

## **Acknowledgements**

Authors acknowledge EU for funding the CHALLENGE project (3C-SiC Hetero-epitaxiALLY grown on silicon compliance substrates and 3C-SiC substrates

for sustainAble wide-band-Gap power devices) within the EU's H2020 framework program for research and innovation under grant agreement n. 720827. The CINECA award under the ISCRA initiative, for the availability of high-performance computing resources and support, is also acknowledged.

## References

- [1] G.L. Harris, Properties of silicon carbide, EMIS n 13, INSPEC, London, 1995. <https://trove.nla.gov.au/version/45147380>.
- [2] G. Kovacs, Micromachined Transducers Sourcebook, McGraw-Hill Science/Engineering/Math, Boston, 1998.
- [3] C.E. Wooddell, Method of Comparing the Hardness of Electric Furnace Products and Natural Abrasives, Trans. Electrochem. Soc. 68 (1935) 111. <https://doi.org/10.1149/1.3493860>.
- [4] A. Fissel, B. Schröter, W. Richter, Low-temperature growth of SiC thin films on Si and 6H-SiC by solid-source molecular beam epitaxy, Appl. Phys. Lett. 66 (1995) 3182. <https://doi.org/10.1063/1.113716>.
- [5] G.R. Fisher, P. Barnes, Towards a unified view of polytypism in silicon carbide, Philos. Mag. B Phys. Condens. Matter; Stat. Mech. Electron. Opt. Magn. Prop. 61 (1990) 217–236. <https://doi.org/10.1080/13642819008205522>.
- [6] A.R. Verma, Polymorphism and polytypism in crystals, John Wiley and Sons, Inc., New York, London, Sydney, 1966. <https://doi.org/10.1002/crat.19660010415>.
- [7] E. Scalise, A. Marzegalli, F. Montalenti, L. Miglio, Temperature-Dependent Stability of Polytypes and Stacking Faults in SiC: Reconciling Theory and Experiments, Phys. Rev. Appl. 12 (2019) 021002. <https://doi.org/10.1103/PhysRevApplied.12.021002>.
- [8] H. Okumura, K. Ohta, G. Feuillet, K. Balakrishnan, S. Chichibu, H. Hamaguchi, P. Hacke, S. Yoshida, Growth and characterization of cubic GaN, J. Cryst. Growth. 178 (1997) 113–133. [https://doi.org/10.1016/S0022-0248\(97\)00084-5](https://doi.org/10.1016/S0022-0248(97)00084-5).
- [9] P.B. Mirkarimi, D.L. Medlin, K.F. McCarty, J.C. Barbour, Growth of cubic BN films on  $\beta$ -SiC by ion-assisted pulsed laser deposition, Appl. Phys. Lett. 66 (1995) 2813–2815. <https://doi.org/10.1063/1.113484>.
- [10] T. Ohno, H. Yamaguchi, S. Kuroda, K. Kojima, T. Suzuki, K. Arai, Direct observation of dislocations propagated from 4H-SiC substrate to epitaxial layer by X-

ray topography, *J. Cryst. Growth*. 260 (2004) 209–216.

<https://doi.org/10.1016/j.jcrysgro.2003.08.065>.

[11] S. Nishino, J.A. Powell, H.A. Will, Production of large-area single-crystal wafers of cubic SiC for semiconductor devices, *Appl. Phys. Lett.* 42 (1983) 460–462.

<https://doi.org/10.1063/1.93970>.

[12] P. Pirouz, C.M. Chorney, T.T. Cheng, J.A. Powell, Lattice Defects in  $\beta$ -SiC Grown Epitaxially On Silicon Substrates, *MRS Proc.* 91 (1987) 399.

<https://doi.org/10.1557/PROC-91-399>.

[13] M.E. Levinshtein, S.L. Rumyantsev, M.S. Shur, *Properties of Advanced Semiconductor Materials: GaN, AlN, InN, BN, SiC, SiGe*, Wiley-interscience publications, New York, 2001.

[14] C.W. Liu, J.C. Sturm, Low temperature chemical vapor deposition growth of  $\beta$ -SiC on (100) Si using methylsilane and device characteristics, *J. Appl. Phys.* 82 (1997) 4558–4565.

<https://doi.org/10.1063/1.366192>.

[15] Y. Ishida, M. Kushibe, T. Takahashi, H. Okumura, S. Yoshida, Investigation of the Relationship between Defects and Electrical Properties of 3C-SiC Epilayers, *Mater. Sci. Forum.* 389–393 (2002) 459–462.

<https://doi.org/10.4028/www.scientific.net/MSF.389-393.459>.

[16] Y. Ishida, M. Kushibe, T. Takahashi, H. Okumura, S. Yoshida, Investigation of the Relationship between Defects and Electrical Properties of 3C-SiC Epilayers, *Mater. Sci. Forum.* 389–393 (2002) 459–462.

<https://doi.org/10.4028/www.scientific.net/MSF.389-393.459>.

[17] M.A. Capano, A.R. Smith, B.C. Kim, E.P. Kvam, S. Tsoi, A.K. Ramdas, J.A. Cooper, Structural Defects and Critical Electric Field in 3C-SiC, *Mater. Sci. Forum.* 527–529 (2006) 431–434.

<https://doi.org/10.4028/www.scientific.net/MSF.527-529.431>.

[18] H. Nagasawa, K. Yagi, T. Kawahara, N. Hatta, M. Abe, Hetero- and homo-epitaxial growth of 3C-SiC for MOS-FETs, *Microelectron. Eng.* 83 (2006) 185–188.

<https://doi.org/10.1016/j.mee.2005.10.046>.

[19] J. Eriksson, M.H. Weng, F. Roccaforte, F. Giannazzo, S. Leone, V. Raineri, Toward an ideal Schottky barrier on 3C-SiC, *Appl. Phys. Lett.* 95 (2009).

<https://doi.org/10.1063/1.3211965>.

[20] T. Kawahara, N. Hatta, K. Yagi, H. Uchida, M. Kobayashi, M. Abe, H. Nagasawa, B. Zippelius, G. Pensl, Correlation between Leakage Current and Stacking Fault Density of p-n Diodes Fabricated on 3C-SiC, *Mater. Sci. Forum.* 645–648 (2010) 339–342.

<https://doi.org/10.4028/www.scientific.net/msf.645-648.339>.

- [21] H. Nagasawa, M. Abe, K. Yagi, T. Kawahara, N. Hatta, Fabrication of high performance 3C-SiC vertical MOSFETs by reducing planar defects, *Phys. Status Solidi Basic Res.* 245 (2008) 1272–1280. <https://doi.org/10.1002/pssb.200844053>.
- [22] S. Nishino, Y. Hazuki, H. Matsunami, T. Tanaka, Chemical Vapor Deposition of Single Crystalline  $\beta$ -SiC Films on Silicon Substrate with Sputtered SiC Intermediate Layer, *J. Electrochem. Soc.* 127 (1980) 2674–2680. <https://doi.org/10.1149/1.2129570>.
- [23] S. Nishino, J.A. Powell, H.A. Will, Production of large-area single-crystal wafers of cubic SiC for semiconductor devices, *Appl. Phys. Lett.* 42 (1983) 460–462. <https://doi.org/10.1063/1.93970>.
- [24] A. Severino, G. D'Arrigo, C. Bongiorno, S. Scalese, F. La Via, G. Foti, Thin crystalline 3C-SiC layer growth through carbonization of differently oriented Si substrates, *J. Appl. Phys.* 102 (2007). <https://doi.org/10.1063/1.2756620>.
- [25] G. Ferro, T. Chassagne, A. Leycuras, F. Cauwet, Y. Monteil, Strain tailoring in 3C-SiC heteroepitaxial layers grown on Si(100), *Chem. Vap. Depos.* 12 (2006) 483–488. <https://doi.org/10.1002/cvde.200506461>.
- [26] C. Long, S.A. Ustin, W. Ho, Structural defects in 3C-SiC grown on Si by supersonic jet epitaxy, *J. Appl. Phys.* 86 (1999) 2509–2515. <https://doi.org/10.1063/1.371085>.
- [27] C. Wen, Y.M. Wang, W. Wan, F.H. Li, J.W. Liang, J. Zou, Nature of interfacial defects and their roles in strain relaxation at highly lattice mismatched 3C -SiC/Si (001) interface, *J. Appl. Phys.* 106 (2009). <https://doi.org/10.1063/1.3234380>.
- [28] B. Yang, H. Zhuang, J. Li, N. Huang, L. Liu, K. Tai, X. Jiang, Defect-induced strain relaxation in 3C-SiC films grown on a (100) Si substrate at low temperature in one step, *CrystEngComm.* 18 (2016) 6817–6823. <https://doi.org/10.1039/c6ce01409g>.
- [29] M. Bosi, C. Ferrari, D. Nilsson, P.J. Ward, 3C-SiC carbonization optimization and void reduction on misoriented Si substrates: From a research reactor to a production scale reactor, *CrystEngComm.* (2016). <https://doi.org/10.1039/c6ce01388k>.
- [30] A. Boulle, D. Dompont, I. Galben-Sandulache, D. Chaussende, Quantitative analysis of diffuse X-ray scattering in partially transformed 3C-SiC single crystals, *J. Appl. Crystallogr.* 43 (2010) 867–875. <https://doi.org/10.1107/S0021889810019412>.
- [31] M. Kitabatake, SiC/Si heteroepitaxial growth, *Thin Solid Films.* 369 (2000) 257–264. [https://doi.org/10.1016/S0040-6090\(00\)00819-1](https://doi.org/10.1016/S0040-6090(00)00819-1).
- [32] A. Severino, C. Bongiorno, N. Piluso, M. Italia, M. Camarda, M. Mauceri, G. Condorelli, M.A. Di Stefano, B. Cafra, A. La Magna, F. La Via, High-quality 6 inch

- (111) 3C-SiC films grown on off-axis (111) Si substrates, *Thin Solid Films*. 518 (2010) S165–S169. <https://doi.org/10.1016/j.tsf.2009.10.080>.
- [33] T. Kreiliger, M. Mauceri, M. Puglisi, F. Mancarella, F. La Via, D. Crippa, W. Kaplan, A. Schöner, A. Marzegalli, L. Miglio, H. von Känel, 3C-SiC Epitaxy on Deeply Patterned Si(111) Substrates, *Mater. Sci. Forum*. 858 (2016) 151–154. <https://doi.org/10.4028/www.scientific.net/MSF.858.151>.
- [34] H. von Känel, L. Miglio, D. Crippa, T. Kreiliger, M. Mauceri, M. Puglisi, F. Mancarella, R. Anzalone, N. Piluso, F. La Via, Defect Reduction in Epitaxial 3C-SiC on Si(001) and Si(111) by Deep Substrate Patterning, *Mater. Sci. Forum*. 821–823 (2015) 193–196. <https://doi.org/10.4028/www.scientific.net/MSF.821-823.193>.
- [35] N. Hatta, T. Kawahara, K. Yagi, H. Nagasawa, S.A. Reshanov, A. Schöner, Reliable Method for Eliminating Stacking Fault on 3C-SiC(001), *Mater. Sci. Forum*. 717–720 (2012) 173–176. <https://doi.org/10.4028/www.scientific.net/MSF.717-720.173>.
- [36] F. La Via, G. D'Arrigo, A. Severino, N. Piluso, M. Mauceri, C. Locke, S.E. Sadow, Patterned substrate with inverted silicon pyramids for 3C-SiC epitaxial growth: A comparison with conventional (001) Si substrate, *J. Mater. Res.* 28 (2013) 94–103. <https://doi.org/10.1557/jmr.2012.268>.
- [37] U. Lindefelt, H. Iwata, S. Öberg, P.R. Briddon, Stacking faults in 3C-,4H-,6H-SiC polytypes investigated by an ab initio supercell method, *Phys. Rev. B*. 67 (2003) 155204. <https://doi.org/10.1103/PhysRevB.67.155204>.
- [38] I. Deretzis, M. Camarda, F. La Via, A. La Magna, Electron backscattering from stacking faults in SiC by means of ab initio quantum transport calculations, *Phys. Rev. B - Condens. Matter Mater. Phys.* 85 (2012) 1–5. <https://doi.org/10.1103/PhysRevB.85.235310>.
- [39] H. Nagasawa, R. Gurunathan, M. Suemitsu, Controlling planar defects in 3C–SiC: Ways to wake it up as a practical semiconductor, *Mater. Sci. Forum*. 821–823 (2015) 108–114. <https://doi.org/10.4028/www.scientific.net/MSF.821-823.108>.
- [40] S. Plimpton, Fast parallel algorithms for short-range molecular dynamics, *J. Comput. Phys.* 117 (1995) 1–19. <https://doi.org/10.1006/jcph.1995.1039>.
- [41] P. Vashishta, R.K. Kalia, A. Nakano, J.P. Rino, Interaction potential for silicon carbide: A molecular dynamics study of elastic constants and vibrational density of states for crystalline and amorphous silicon carbide, *J. Appl. Phys.* 101 (2007) 103515. <https://doi.org/10.1063/1.2724570>.
- [42] J. Nord, K. Albe, P. Erhart, K. Nordlund, Modelling of compound semiconductors: Analytical bond-order potential for gallium, nitrogen and gallium

nitride, *J. Phys. Condens. Matter.* 15 (2003) 5649–5662.

<https://doi.org/10.1088/0953-8984/15/32/324>.

[43] A. Sarikov, A. Marzegalli, L. Barbisan, E. Scalise, F. Montalenti, L. Miglio, Molecular dynamics simulations of extended defects and their evolution in 3C–SiC by different potentials, *Model. Simul. Mater. Sci. Eng.* 28 (2020) 015002.

<https://doi.org/10.1088/1361-651X/ab50c7>.

[44] W. Shinoda, M. Shiga, M. Mikami, Rapid estimation of elastic constants by molecular dynamics simulation under constant stress, *Phys. Rev. B - Condens. Matter Mater. Phys.* 69 (2004) 16–18. <https://doi.org/10.1103/PhysRevB.69.134103>.

[45] A. Stukowski, Visualization and analysis of atomistic simulation data with OVITO-the Open Visualization Tool, *Model. Simul. Mater. Sci. Eng.* 18 (2010).

<https://doi.org/10.1088/0965-0393/18/1/015012>.

[46] J. P. Hirth, J. Lothe, *Theory of Dislocations*, Krieger Publishing Company, 1982.

[47] L. Tong, M. Mehregany, L.G. Matus, Mechanical properties of 3C silicon carbide, *Appl. Phys. Lett.* 60 (1992) 2992–2994. <https://doi.org/10.1063/1.106786>.

[48] W. Cai, V. V. Bulatob, J. Chang, J. Li, S. Tip, Periodic image effects in dislocation modelling, *Philos. Mag.* 83 (2003) 539–567.

<https://doi.org/10.1080/0141861021000051109>.

[49] A.M. Andrews, J.S. Speck, A.E. Romanov, M. Bobeth, W. Pompe, Modeling cross-hatch surface morphology in growing mismatched layers, *J. Appl. Phys.* 91 (2002) 1933–1943. <https://doi.org/10.1063/1.1428091>.

[50] J.P. Perdew, K. Burke, M. Ernzerhof, Generalized Gradient Approximation Made Simple, *Phys. Rev. Lett.* 77 (1996) 3865–3868.

<https://doi.org/10.1103/PhysRevLett.77.3865>.

[51] P. Giannozzi, S. Baroni, N. Bonini, M. Calandra, R. Car, C. Cavazzoni, D. Ceresoli, G.L. Chiarotti, M. Cococcioni, I. Dabo, A. Dal Corso, S. De Gironcoli, S. Fabris, G. Fratesi, R. Gebauer, U. Gerstmann, C. Gougoussis, A. Kokalj, M. Lazzeri, L. Martin-Samos, N. Marzari, F. Mauri, R. Mazzarello, S. Paolini, A. Pasquarello, L. Paulatto, C. Sbraccia, S. Scandolo, G. Sclauzero, A.P. Seitsonen, A. Smogunov, P. Umari, R.M. Wentzcovitch, QUANTUM ESPRESSO: A modular and open-source software project for quantum simulations of materials, *J. Phys. Condens. Matter.* 21 (2009). <https://doi.org/10.1088/0953-8984/21/39/395502>.

[52] F. Han, Projector-Augmented Plane-Wave Method, in: *Probl. Solid State Phys. with Solut.*, WORLD SCIENTIFIC, 2011: pp. 391–396.

[https://doi.org/10.1142/9789814365031\\_0023](https://doi.org/10.1142/9789814365031_0023).

- [53] S. Grimme, Semiempirical GGA-type density functional constructed with a long-range dispersion correction, *J. Comput. Chem.* 27 (2006) 1787–1799. <https://doi.org/10.1002/jcc.20495>.
- [54] Y. Yao, Y. Kanai, Plane-wave pseudopotential implementation and performance of SCAN meta-GGA exchange-correlation functional for extended systems, *J. Chem. Phys.* 146 (2017) 224105. <https://doi.org/10.1063/1.4984939>.
- [55] J. Zou, D.J.H. Cockayne, Theoretical consideration of equilibrium dissociation geometries of 60° misfit dislocations in single semiconductor heterostructures, *J. Appl. Phys.* 77 (1995) 2448–2453. <https://doi.org/10.1063/1.358772>.
- [56] A.M. Sanchez, J.A. Gott, H.A. Fonseca, Y. Zhang, H. Liu, R. Beanland, Stable Defects in Semiconductor Nanowires, *Nano Lett.* 18 (2018) 3081–3087. <https://doi.org/10.1021/acs.nanolett.8b00620>.
- [57] A. Sarikov, A. Marzegalli, L. Barbisan, F. Montalenti, L. Miglio, Structure and stability of partial dislocation complexes in 3C-SiC by molecular dynamics simulations, *Materials (Basel)*. 12 (2019). <https://doi.org/10.3390/ma12183027>.
- [58] R. Vasiliauskas, M. Marinova, M. Syväjärvi, E.K. Polychroniadis, R. Yakimova, Polytype transformation and structural characteristics of 3C-SiC on 6H-SiC substrates, *J. Cryst. Growth*. 395 (2014) 109–115. <https://doi.org/10.1016/j.jcrysgro.2014.03.021>.
- [59] K. Tanaka, M. Kohyama, M. Iwasa, The Variety of Structures of the  $\Sigma=3$  Incoherent Twin Boundary in  $\beta$ -SiC, *Mater. Sci. Forum*. 294–296 (1998) 187–190. <https://doi.org/10.4028/www.scientific.net/MSF.294-296.187>.
- [60] K. Tanaka, M. Kohyama, Experimental and theoretical study of  $\Sigma = 3$  incoherent twin boundary in  $\beta$ -SiC, *Philos. Mag. A Phys. Condens. Matter, Struct. Defects Mech. Prop.* 82 (2002) 215–229. <https://doi.org/10.1080/01418610208239595>.
- [61] M. Lancin, C. Ragaru, C. Godon, Atomic structure and core composition of partial dislocations and dislocation fronts in  $\beta$ -SiC by high-resolution transmission electron microscopy, *Philos. Mag. B Phys. Condens. Matter; Stat. Mech. Electron. Opt. Magn. Prop.* 81 (2001) 1633–1647. <https://doi.org/10.1080/13642810108223108>.
- [62] B. Chen, J. Chen, T. Sekiguchi, T. Ohyanagi, H. Matsuhata, A. Kinoshita, H. Okumura, F. Fabbri, Electrical activities of stacking faults and partial dislocations in 4H-SiC homoepitaxial films, *Superlattices Microstruct.* 45 (2009) 295–300. <https://doi.org/10.1016/j.spmi.2008.10.021>.
- [63] S. Ha, M. Skowronski, H. Lendenmann, Nucleation sites of recombination-enhanced stacking fault formation in silicon carbide p-i-n diodes, *J. Appl. Phys.* 96 (2004) 393–398. <https://doi.org/10.1063/1.1756218>.

- [64] S.I. Maximenko, T.S. Sudarshan, Stacking fault nucleation sites in diffused 4H-SiC p-i-n diodes, *J. Appl. Phys.* 97 (2005). <https://doi.org/10.1063/1.1872196>.
- [65] H. Nagasawa, K. Yagi, T. Kawahara, N. Hatta, M. Abe, A. Schöner, M. Bakowski, P. Ericsson, G. Pensl, Challenges for Improving the Crystal Quality of 3C-SiC Verified with MOSFET Performance, *Mater. Sci. Forum.* 600–603 (2009) 89–94. <https://doi.org/10.4028/www.scientific.net/MSF.600-603.89>.
- [66] F. Bernardini, L. Colombo, Interaction of doping impurities with the 30° partial dislocations in SiC: An ab initio investigation, *Phys. Rev. B - Condens. Matter Mater. Phys.* 72 (2005) 1–10. <https://doi.org/10.1103/PhysRevB.72.085215>.
- [67] P. Käckell, J. Furthmüller, F. Bechstedt, Polytypic transformations in sic: an ab initio study, *Phys. Rev. B - Condens. Matter Mater. Phys.* 60 (1999) 13261–13264. <https://doi.org/10.1103/PhysRevB.60.13261>.
- [68] P. Tanner, A. Iacopi, H.P. Phan, S. Dimitrijević, L. Hold, K. Chaik, G. Walker, D.V. Dao, N.T. Nguyen, Excellent Rectifying Properties of the n-3C-SiC/p-Si Heterojunction Subjected to High Temperature Annealing for Electronics, MEMS, and LED Applications, *Sci. Rep.* 7 (2017) 3. <https://doi.org/10.1038/s41598-017-17985-9>.